Transmission stability and Raman-induced amplitude dynamics in multichannel soliton-based optical waveguide systems

Avner Peleg[a,*], Quan M. Nguyen[b], Thinh P. Tran[c]

[a]*Department of Exact Sciences, Afeka College of Engineering, Tel Aviv 69988, Israel*
[b]*Department of Mathematics, International University, Vietnam National University-HCMC, Ho Chi Minh City, Vietnam*
[c]*Department of Theoretical Physics, University of Science, Vietnam National University-HCMC, Ho Chi Minh City, Vietnam*

Abstract

We study transmission stability and dynamics of pulse amplitudes in N-channel soliton-based optical waveguide systems, taking into account second-order dispersion, Kerr nonlinearity, delayed Raman response, and frequency dependent linear gain-loss. We carry out numerical simulations with systems of N coupled nonlinear Schrödinger (NLS) equations and compare the results with the predictions of a simplified predator-prey model for Raman-induced amplitude dynamics. Coupled-NLS simulations for single-fiber transmission with $2 \leq N \leq 4$ frequency channels show stable oscillatory dynamics of soliton amplitudes at short-to-intermediate distances, in excellent agreement with the predator-prey model's predictions. However, at larger distances, we observe transmission destabilization due to resonant formation of radiative sidebands, which is caused by Kerr nonlinearity. The presence of linear gain-loss in a single fiber leads to a limited increase in transmission stability. Significantly stronger enhancement of transmission stability is achieved in a nonlinear N-waveguide coupler due to efficient suppression of radiative sideband generation by the linear gain-loss. As a result, the distances along which stable Raman-induced dynamics of soliton amplitudes is observed are significantly larger in the waveguide coupler system

---

[*]Corresponding author
 Email address: `avpeleg@gmail.com` (Avner Peleg)

compared with the single-fiber system.

1. Introduction

Transmission of information in broadband optical waveguide links can be significantly enhanced by launching many pulse sequences through the same waveguide [1, 2, 3, 4, 5]. Each pulse sequence propagating through the waveguide is characterized by the central frequency of its pulses, and is therefore called a frequency channel. Applications of these multichannel systems, which are also known as wavelength-division-multiplexed (WDM) systems, include fiber optics transmission lines [2, 3, 4, 5], data transfer between computer processors through silicon waveguides [6, 7, 8], and multiwavelength lasers [9, 10, 11, 12]. Since pulses from different frequency channels propagate with different group velocities, interchannel pulse collisions are very frequent, and can therefore lead to error generation and cause severe transmission degradation [1, 2, 3, 4, 5, 13, 14].

In the current paper, we study pulse propagation in broadband multichannel optical fiber systems with N frequency channels, considering optical solitons as an example for the pulses. The two main processes affecting interchannel soliton collisions in these systems are due to the fiber's instantaneous nonlinear response (Kerr nonlinearity) and delayed Raman response. The only effects of Kerr nonlinearity on a single interchannel collision between two isolated solitons in a long optical fiber are a phase shift and a position shift, which scale as $1/\Delta\beta$ and $1/\Delta\beta^2$, respectively, where $\Delta\beta$ is the difference between the frequencies of the colliding solitons [15, 14, 16]. Thus, in this long fiber setup, the amplitude, frequency, and shape of the solitons do not change due to the collision. However, the situation changes, once the finite length of the fiber and the finite separation between the solitons are taken into account [17]. In this case, the collision

2

leads to emission of small amplitude waves (continuous radiation) with peak power that is also inversely proportional to $\Delta\beta$. The emission of continuous radiation in many collisions in an N-channel transmission system can eventually lead to pulse-shape distortion and as a result, to transmission destabilization [17]. The main effect of delayed Raman response on single-soliton propagation in an optical fiber is an $O(\epsilon_R)$ frequency downshift, where ϵ_R is the Raman coefficient [18, 19, 20]. This Raman-induced self frequency shift is a result of energy transfer from high frequency components of the pulse to lower frequency components. The main effect of delayed Raman response on an interchannel two-soliton collision is an $O(\epsilon_R)$ amplitude shift, which is called Raman-induced crosstalk [21, 22, 23, 24, 25, 26, 27, 16, 28]. It is a result of energy transfer from the high frequency pulse to the low frequency one. The amplitude shift is accompanied by an $O(\epsilon_R/\Delta\beta)$ collision-induced frequency downshift (Raman cross frequency shift) and by emission of continuous radiation [23, 29, 25, 26, 27, 16, 28]. Note that the Raman-induced amplitude shift in a single collision is independent of the magnitude of the frequency difference between the colliding solitons. Consequently, the cumulative amplitude shift experienced by a given pulse in an N-channel transmission line is proportional to N^2, a result that is valid for linear transmission [21, 22, 30, 31], conventional soliton transmission [23, 24, 25, 27], and dispersion-managed soliton transmission [26]. Thus, in a 100-channel system, for example, Raman crosstalk effects are larger by a factor of 2.5×10^3 compared with a two-channel system operating at the same bit rate per channel. For this reason, Raman-induced crosstalk is considered to be one of the most important processes affecting the dynamics of optical pulse amplitudes in broadband fiber optics transmission lines [1, 21, 22, 2, 31, 32, 33, 34, 35].

The first studies of Raman crosstalk in multichannel fiber optics transmission focused on the dependence of the energy shifts on the total number of channels [21], as well as on the impact of energy depletion and group velocity dispersion on amplitude dynamics [30, 36]. Later studies turned their attention to the interplay between bit-pattern randomness and Raman crosstalk in on-off-keyed (OOK) transmission, and showed that this interplay leads to lognormal

statistics of pulse amplitudes [22, 31, 27, 16, 32, 37]. This finding means that the nth normalized moments of the probability density function (PDF) of pulse amplitudes grow exponentially with both propagation distance and n^2. Furthermore, in studies of soliton-based multichannel transmission, it was found that the nth normalized moments of the PDFs of the Raman self and cross frequency shifts also grow exponentially with propagation distance and n^2 [33, 34]. The exponential growth of the normalized moments of pulse parameter PDFs can be interpreted as intermittent dynamics, in the sense that the statistics of the amplitude and frequency is very sensitive to bit-pattern randomness [33, 34, 38]. Moreover, it was shown in Refs. [33, 34, 35] that this intermittent dynamics has important practical consequences in massive multichannel transmission, by leading to relatively high bit-error-rate values at intermediate and large propagation distances. Additionally, the different scalings and statistics of Raman-induced and Kerr-induced effects lead to loss of scalability in these systems [35].

One of the ways to overcome the detrimental effects of Raman crosstalk on massive OOK multichannel transmission is by employing encoding schemes, which are less susceptible to these effects. The phase shift keying (PSK) scheme, in which the information is encoded in the phase difference between adjacent pulses, is among the most promising encoding methods, and has thus become the focus of intensive research [39, 40]. Since in PSK transmission the information is encoded in the phase, the amplitude patterns are deterministic, and as a result, the Raman-induced amplitude dynamics is also approximately deterministic. A key question about this deterministic dynamics concerns the possibility to achieve stable steady-state transmission with nonzero predetermined amplitude values in all channels. In Ref. [30], it was demonstrated that this is not possible in unamplified optical fiber lines. However, the experiments in Refs. [41, 42] showed that the situation is very different in amplified multichannel transmission. More specifically, it was found that the introduction of amplification enables transmission stabilization and significant reduction of the cumulative Raman crosstalk effects. In Ref. [43], we provided a dynamical explanation for the stabilization of PSK soliton-based multichannel transmission,

by demonstrating that the Raman-induced amplitude shifts can be balanced by an appropriate choice of amplifier gain in different channels. Our approach was based on showing that the collision-induced dynamics of soliton amplitudes in an N-channel system can be described by a relatively simple N-dimensional predator-prey model. Furthermore, we obtained the Lyapunov function for the predator-prey model and used it to show that stable transmission with nonzero amplitudes in all channels can be realized by overamplification of high frequency channels and underamplification of low frequency channels.

All the results in Ref. [43] were obtained with the N-dimensional predator-prey model, which is based on several simplifying assumptions, whose validity might break down with increasing number of channels or at large propagation distances. In particular, the predator-prey model neglects high-order effects due to radiation emission, intrasequence interaction, and temporal inhomogeneities. These effects can lead to pulse shape distortion and eventually to transmission destabilization (see, for example, Ref. [17]). The distortion of the solitons shapes can also lead to the breakdown of the predator-prey model description at large distances. For example, the relation between the onset of pulse pattern distortion and the breakdown of the simplified model for dynamics of pulse amplitude was noted (but not quantified) in studies of crosstalk induced by nonlinear gain or loss [44, 45, 46]. In contrast, the complete propagation model, which consists of a system of N perturbed coupled nonlinear Schrödinger (NLS) equations, fully incorporates the effects of radiation emission, intrachannel interaction, and temporal inhomogeneities. Thus, in order to check whether stable long-distance multichannel transmission can indeed be realized by a proper choice of linear amplifier gain, it is important to carry out numerical simulations with the full coupled-NLS model.

In the current paper, we take on this important task. For this purpose, we employ perturbed coupled-NLS models, which take into account the effects of second-order dispersion, Kerr nonlinearity, delayed Raman response, and frequency dependent linear gain-loss. We perform numerical simulations with the coupled-NLS models with $2 \leq N \leq 4$ frequency channels for two main trans-

5

mission setups. In the first setup, the soliton sequences propagate through a single optical fiber, while in the second setup, the sequences propagate through a waveguide coupler. We then analyze the simulations results in comparison with the predictions of the predator-prey model of Ref. [43], looking for processes leading to transmission stabilization and destabilization. The coupled-NLS simulations for single-fiber transmission show that at short-to-intermediate distances soliton amplitudes exhibit stable oscillatory dynamics, in excellent agreement with the predator-prey model's predictions. These results mean that radiation emission and intrachannel interaction effects can indeed be neglected at short-to-intermediate distances. However, at larger distances, we observe transmission destabilization due to formation of radiative sidebands, which is caused by the effects of Kerr nonlinearity on interchannel soliton collisions. We also find that the radiative sidebands for the jth soliton sequence form near the frequencies $\beta_k(z)$ of the solitons in the neighboring frequency channels. Additionally, we find that the presence of frequency dependent linear gain-loss in a single fiber leads to a moderate increase in the distance along which stable transmission is observed. The limited enhancement of transmission stability in a single fiber is explained by noting that in this case one cannot employ strong linear loss at the frequencies of the propagating solitons, and therefore, one cannot efficiently suppress the formation of the radiative sidebands.

A stronger enhancement of transmission stability might be achieved in a nonlinear waveguide coupler, consisting of N nearby waveguides. Indeed, in this case one might expect to achieve a more efficient suppression of radiative sideband generation by employing relatively strong linear loss outside of the central amplification frequency interval for each of the N waveguides in the waveguides coupler. To test this prediction, we carry out numerical simulations with the coupled-NLS model for propagation in the waveguide coupler. The coupled-NLS simulations show that transmission stability and the validity of the predator-prey model's predictions in the waveguide coupler system are extended to significantly larger distances compared with the distances in the single-fiber system. Furthermore, the simulations for the waveguide coupler

6

show that no radiative sidebands form throughout the propagation. Based on these observations we conclude that the enhanced transmission stability in the waveguide coupler is a result of the efficient suppression of radiative sideband generation by the frequency dependent linear gain-loss in this setup.

We consider optical solitons as an example for the pulses carrying the information for the following reasons. First, due to the integrability of the unperturbed NLS equation and the shape-preserving property of NLS solitons, derivation of the predator-prey model for Raman-induced amplitude dynamics is done in a rigorous manner [43]. Second, the soliton stability and shape-preserving property make soliton-based transmission in broadband fiber optics links advantageous compared with other transmission methods [1, 3, 13, 47]. Third, as mentioned above, the Raman-induced energy exchange in pulse collisions is similar in linear transmission, conventional soliton transmission, and dispersion-managed soliton transmission. Thus, even though pulse dynamics in these different transmission systems is different, analysis of soliton-based transmission stabilization and destabilization might give a rough idea about the processes leading to stabilization and destabilization of the optical pulse sequences in other transmission setups.

The remainder of the paper is organized as follows. In Section 2, we present the coupled-NLS model for N-channel transmission in a single fiber together with the N-dimensional predator-prey model for Raman-induced dynamics of pulse amplitudes. We then review the results of Ref. [43] for stability analysis of the equilibrium states of the predator-prey model. In Section 3, we present the results of numerical simulations with the coupled-NLS model for single-fiber multichannel transmission and analyze these results in comparison with the predictions of the predator-prey model. In Section 4, we present the coupled-NLS model for pulse propagation in a nonlinear N-waveguide coupler. We then analyze the results of numerical simulations with this model and compare the results with the predator-prey model's predictions. Our conclusions are presented in Section 5. In Appendix A, we discuss the method for determining the stable propagation distance from the results of the numerical simulations.

7

2. The propagation model for single-fiber transmission and the predator-prey model for amplitude dynamics

We consider propagation of pulses of light in a single-fiber N-channel transmission link, taking into account second-order dispersion, Kerr nonlinearity, delayed Raman response, and frequency-dependent linear loss or gain. The net linear gain-loss is the difference between amplifier gain and fiber loss, where we assume that the gain is provided by distributed Raman amplification [48, 49]. In addition, we assume that the frequency difference $\Delta\beta$ between adjacent channels is much larger than the spectral width of the pulses, which is the typical situation in many soliton-based WDM systems [14, 50, 51, 52, 53]. Under these assumptions, the propagation is described by the following system of N perturbed coupled-NLS equations [54]:

$$i\partial_z\psi_j + \partial_t^2\psi_j + 2|\psi_j|^2\psi_j + 4\sum_{k=1}^{N}(1-\delta_{jk})|\psi_k|^2\psi_j = i\mathcal{F}^{-1}(g(\omega)\hat{\psi}_j)/2$$

$$-\epsilon_R\psi_j\partial_t|\psi_j|^2 - \epsilon_R\sum_{k=1}^{N}(1-\delta_{jk})\left[\psi_j\partial_t|\psi_k|^2 + \psi_k\partial_t(\psi_j\psi_k^*)\right], \tag{1}$$

where ψ_j is proportional to the envelope of the electric field of the jth sequence, $1 \leq j \leq N$, z is propagation distance, and t is time [55]. In Eq. (1), ϵ_R is the Raman coefficient, $g(\omega)$ is the net frequency dependent linear gain-loss function [56], $\hat{\psi}$ is the Fourier transform of ψ with respect to time, $\mathcal{F}^{-1}$ stands for the inverse Fourier transform, and δ_{jk} is the Kronecker delta function. The second term on the left hand side of Eq. (1) describes second-order dispersion effects, while the third and fourth terms represent intrachannel and interchannel interaction due to Kerr nonlinearity. The first term on the right hand side of Eq. (1) describes the effects of frequency dependent linear gain or loss, the second corresponds to Raman-induced intrachannel interaction, while the third and fourth terms describe Raman-induced interchannel interaction.

The form of the net frequency dependent linear gain-loss function $g(\omega)$ is chosen so that Raman crosstalk and radiation emission effects are suppressed. More specifically, $g(\omega)$ is equal to a value g_j, required to balance Raman-induced

amplitude shifts, inside a frequency interval of width W centered about the initial frequency of the jth-channel solitons $\beta_j(0)$, and is equal to a negative value g_L elsewhere. Thus, $g(\omega)$ is given by:

$$g(\omega) = \begin{cases} g_j & \text{if } \beta_j(0) - W/2 < \omega \le \beta_j(0) + W/2 \text{ for } 1 \le j \le N, \\ g_L & \text{elsewhere,} \end{cases} \qquad (2)$$

where $g_L < 0$. The width W in Eq. (2) satisfies $1 < W \le \Delta\beta$, where $\Delta\beta = \beta_{j+1}(0) - \beta_j(0)$ for $1 \le j \le N-1$. Note that the actual values of the g_j coefficients are determined by the predator-prey model for collision-induced amplitude dynamics, such that amplitude shifts due to Raman crosstalk are compensated for by the linear gain-loss. The value of g_L is determined such that instability due to radiation emission is mitigated. In addition, the value of W is determined by the following two factors. First, we require $W \gg 1$, such that the effects of the strong linear loss g_L on the soliton patterns and on the collision-induced amplitude dynamics are relatively small even at large distances. Second, we typically require $W < \Delta\beta$, such that instability due to radiation emission is effectively mitigated. In practice, we determine the values of g_L and W by carrying out numerical simulations with the coupled-NLS model (1), while looking for the set of values, which yields the longest stable propagation distance. Our simulations show that the optimal g_L value is around 0.5, while W should satisfy $W \ge 10$. Figure 1 illustrates a typical linear gain-loss function $g(\omega)$ for a two-channel system with $g_1 = -0.0045$, $g_2 = 0.0045$, $g_L = -0.5$, $\beta_1(0) = -7.5$, $\beta_2(0) = 7.5$, and $W = 10$. These parameter values are used in the numerical simulations, whose results are shown in Fig. 4(a).

In the current paper we study soliton-based transmission systems, and therefore the optical pulses in the jth frequency channel are fundamental solitons of the unperturbed NLS equation $i\partial_z \psi_j + \partial_t^2 \psi_j + 2|\psi_j|^2 \psi_j = 0$. The envelopes of these solitons are given by $\psi_{sj}(t,z) = \eta_j \exp(i\chi_j)\text{sech}(x_j)$, where $x_j = \eta_j (t - y_j - 2\beta_j z)$, $\chi_j = \alpha_j + \beta_j(t - y_j) + (\eta_j^2 - \beta_j^2) z$, and the four parameters η_j, β_j, y_j, and α_j are related to the soliton amplitude, frequency (and group velocity), position, and phase, respectively. The assumption of a large fre-
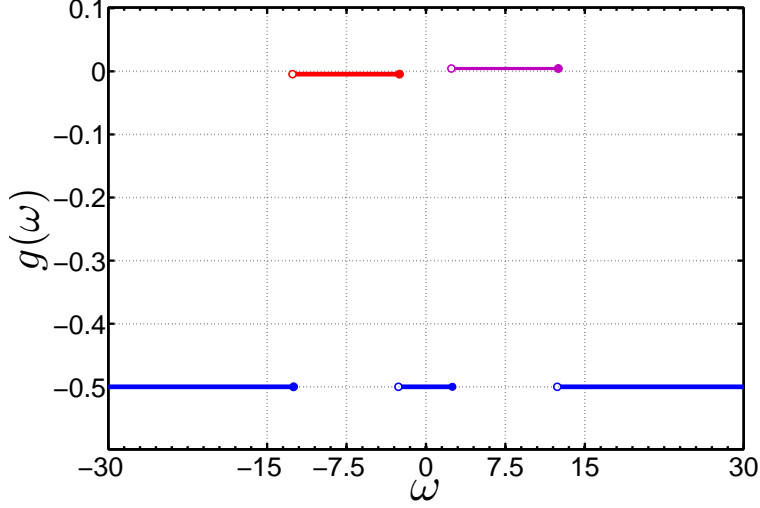
Figure 1: (Color online) An example for the frequency-dependent linear gain-loss function $g(\omega)$, described by Eq. (2), in a two-channel system.

quency (and group velocity) difference between adjacent channels, means that $|\beta_j - \beta_k| \gg 1$ for $1 \le j \le N$, $1 \le k \le N$, and $j \ne k$. As a result of the large group velocity difference, the solitons undergo a large number of intersequence collisions. The Raman-induced crosstalk during these collisions can lead to significant amplitude and frequency shifts, which can in turn lead to severe transmission degradation.

In Ref. [43], we showed that the dynamics of soliton amplitudes in an N-channel system can be approximately described by an N-dimensional predator-prey model. The derivation of the predator-prey model was based on the following simplifying assumptions. (1) The soliton sequences are deterministic in the sense that all time slots are occupied and each soliton is located at the center of a time slot of width T, where $T \gg 1$. In addition, the amplitudes are equal for all solitons from the same sequence, but are not necessarily equal for solitons from different sequences. This setup corresponds, for example, to return-to-zero PSK transmission. (2) The sequences are either (a) infinitely long, or (b) subject to periodic temporal boundary conditions. Setup (a) is an approximation for long-haul transmission systems, while setup (b) is an approximation for closed

fiber-loop experiments. (3) The linear gain-loss coefficients g_j in the frequency intervals $(\beta_j(0) - W/2 < \omega \leq \beta_j(0) + W/2]$, defined in Eq. (2), are determined by the difference between distributed amplifier gain and fiber loss. In particular, for some channels this difference can be slightly positive, resulting in small net gain, while for other channels this difference can be slightly negative, resulting in small net loss. (4) Since $T \gg 1$, the solitons in each sequence are temporally well-separated. As a result, intrachannel interaction is exponentially small and is neglected. (5) The Raman coefficient and the reciprocal of the frequency spacing satisfy $\epsilon_R \ll 1/\Delta\beta \ll 1$. Consequently, high-order effects due to radiation emission are neglected, in accordance with the analysis of the single-collision problem [16, 23, 24, 25, 26, 27, 28].

By assumptions (1)-(5), the propagating soliton sequences are periodic, and as a result, the amplitudes of all pulses in a given sequence undergo the same dynamics. Taking into account collision-induced amplitude shifts due to delayed Raman response, and single-pulse amplitude changes due to linear gain-loss, we obtain the following equation for amplitude dynamics of jth-channel solitons [43]:

$$\frac{d\eta_j}{dz} = \eta_j \left[g_j + C \sum_{k=1}^{N} (k-j) f(|j-k|) \eta_k \right], \tag{3}$$

where $C = 4\epsilon_R \Delta\beta/T$, and $1 \leq j \leq N$. The coefficients $f(|j-k|)$ on the right hand side of Eq. (3) are determined by the frequency dependence of the Raman gain. In particular, for the commonly used triangular approximation for the Raman gain curve [1, 21], in which the gain is a piecewise linear function of the frequency, $f(|j-k|) = 1$ for $1 \leq j \leq N$ and $1 \leq k \leq N$ [43].

In WDM systems it is often desired to achieve steady state transmission, in which pulse amplitudes in all channels are equal and constant (independent of z) [1]. We therefore look for a steady state of the system (3) in the form $\eta_j^{(eq)} = \eta > 0$ for $1 \leq j \leq N$, where η is the desired equilibrium amplitude value. This yields the following expression for the g_j:

$$g_j = -C\eta \sum_{k=1}^{N} (k-j) f(|j-k|). \tag{4}$$

11

Thus, in order to maintain steady-state transmission with equal amplitudes in all channels, high-frequency channels should be overamplified and low-frequency channels should be underamplified, compared with central frequency channels. Substituting Eq. (4) into Eq. (3), we obtain the following model for amplitude dynamics [43]:

$$\frac{d\eta_j}{dz} = C\eta_j \sum_{k=1}^{N} (k-j)f(|j-k|)(\eta_k - \eta), \tag{5}$$

which has the form of a predator-prey model for N species [57].

The steady states of the predator-prey model (5) with nonzero amplitudes in all channels are determined by solving the following system of linear equations:

$$\sum_{k=1}^{N} (k-j)f(|j-k|)(\eta_k^{(eq)} - \eta) = 0, \qquad 1 \le j \le N. \tag{6}$$

The trivial solution of Eq. (6), i.e., the solution with $\eta_k^{(eq)} = \eta > 0$ for $1 \le k \le N$, corresponds to steady state transmission with equal nonzero amplitudes. Note that the coefficients $(k-j)f(|j-k|)$ in Eq. (6) are antisymmetric with respect to the interchange of j and k. As a result, for WDM systems with an odd number of channels, Eq. (6) has infinitely many nontrivial solutions, which correspond to steady states of the predator-prey model (5) with unequal nonzero amplitudes. This is also true for WDM systems with an even number of channels, provided that the Raman gain is described by the triangular approximation [43].

The stability of all the steady states with nonzero amplitudes, $\eta_j = \eta_j^{(eq)} > 0, 1 \le j \le N$, was established in Ref. [43], by showing that the function

$$V_L(\boldsymbol{\eta}) = \sum_{j=1}^{N} \left[\eta_j - \eta_j^{(eq)} + \eta_j^{(eq)} \ln\left(\frac{\eta_j^{(eq)}}{\eta_j}\right) \right], \tag{7}$$

where $\boldsymbol{\eta} = (\eta_1, \ldots, \eta_j, \ldots, \eta_N)$, is a Lyapunov function for the predator-prey model (5). This stability was found to be independent of the $f(|j-k|)$ values, i.e., of the specific details of the approximation to the Raman gain curve. Furthermore, since $dV_L/dz = 0$ along trajectories of (5), rather than $dV_L/dz < 0$,

typical dynamics of the amplitudes $\eta_j(z)$ for input amplitudes that are off the steady state value is oscillatory [43]. This behavior also means that the steady states with nonzero amplitudes in all channels are nonlinear centers of Eq. (5) [58].

3. Numerical simulations for single-fiber transmission

The predator-prey model, described in section 2, is based on several simplifying assumptions, whose validity might break down with increasing number of channels or at large propagation distances. In particular, the predator-prey model neglects radiation emission and modulation instability, intrasequence interaction, and deviations from the assumed periodic form of the soliton sequences. These effects can lead to instabilities and pulse-pattern corruption, and also to the breakdown of the predator-prey model description (see, for example Refs. [44, 45, 46], for the case of crosstalk induced by nonlinear gain or loss). In contrast, the coupled-NLS model (1) provides a fuller description of the propagation, which includes all these effects. Thus, in order to check the predictions of the predator-prey model (5) for stable dynamics of soliton amplitudes and the possibility to realize stable long-distance multichannel soliton-based transmission, it is important to carry out numerical simulations with the full coupled-NLS model.

In the current section, we first present numerical simulations with the system (1) without the Raman and the linear gain-loss terms. We then present a comparison between simulations with the full coupled-NLS model (1) with the Raman term and the linear gain-loss profile (2) and the predictions of the predator-prey model (5) for collision-induced amplitude dynamics. We conclude the section by analyzing pulse-pattern deterioration at large distances, as observed in the full coupled-NLS simulations.

The coupled-NLS system (1) is numerically solved using the split-step method with periodic boundary conditions [1]. The use of periodic boundary conditions means that the numerical simulations describe pulse dynamics in a closed fiber

loop. The initial condition is in the form of N periodic sequences of $2J$ solitons with initial amplitudes $\eta_j(0)$, initial frequencies $\beta_j(0)$, and initial zero phases:

$$\psi_j(t,0) = \sum_{k=-J}^{J-1} \frac{\eta_j(0)\exp\{i\beta_j(0)[t-(k+1/2)T-\delta_j]\}}{\cosh\{\eta_j(0)[t-(k+1/2)T-\delta_j]\}}, \qquad (8)$$

where $1 \leq j \leq N$. The coefficients δ_j in Eq. (8) correspond to the initial position shift of the pulses in the jth sequence relative to pulses located at $(k+1/2)T$ for $-J \leq k \leq J-1$. We simulate multichannel transmission with two, three, and four channels and two solitons in each channel. Thus, $2 \leq N \leq 4$ and $J = 1$ are used in our numerical simulations. To maximize the stable propagation distance, we choose $\beta_1(0)$=-$\beta_2(0)$ for a two-channel system; $\beta_1(0)$=-$\beta_3(0)$, $\beta_2(0) = 0$ for a three-channel system; and $\beta_1(0)$=-$\beta_4(0)$, $\beta_2(0)$=-$\beta_3(0)$ for a four-channel system. In addition, we take $\delta_j = (j-1)T/N$ for $1 \leq j \leq N$. These choices are based on extensive numerical simulations with Eq. (1) and different values of $\beta_j(0)$ and δ_j.

In the numerical simulations, we consider as a concrete example transmission at a bit-rate $B = 12.5$ Gb/s per channel with the following physical parameter values [59]. The pulse width and time slot width are $\tau = 5$ ps and $\tilde{T} = 80$ ps, and the frequency spacing is taken as $\Delta\nu = 0.48$ THz for $N = 2, 3$, and 4 channels. Thus, the total bandwidth of the system is smaller than 13.2 THz, and all channels lie within the main body of the Raman gain curve. The values of the dimensionless parameters for this system are $\epsilon_R = 0.0012$, $T = 16$, and $\Delta\beta = 15$ for $N = 2, 3, 4$. Assuming $\tilde{\beta}_2 = -4$ ps^{2}km^{-1} and $\gamma = 4$ W^{-1}km^{-1} for the second-order dispersion and Kerr nonlinearity coefficients, the soliton peak power is $P_0 = 40$ mW. Tables 1 and 2 summarize the values of the dimensionless and dimensional physical parameters used in the simulations. In these tables, W and $\tilde{W}$ stand for the dimensionless and dimensional width of the linear gain-loss function $g(\omega)$ in Eq. (2), while z_s and X_s correspond to the dimensionless and dimensional distance along which stable propagation is observed.

Note that the Kerr nonlinearity terms appearing in Eq. (1) are nonperturbative. Even though these terms are not expected to affect the shape, amplitude,

14

Table 1: The dimensionless parameters

№	N	ϵ_R	T	$\Delta\beta$	W	g_L	z_s	Figures
1	2	0.0012	16	15	10	-0.5	950	1, 4(a), 5(a)-(b)
2	2	0	16	15	0	0	550	2(a)-(b)
3	2	0.0012	16	15	10	-0.5	11200	8(a), 9(a)-(b)
4	3	0	16	15	0	0	510	2(c)-(d)
5	3	0.0012	16	15	10	-0.5	620	4(b), 5(c)-(d)
6	3	0.0012	16	15	10	-0.5	12050	8(b), 9(c)-(d)
7	4	0	16	15	0	0	340	2(e)-(f)
8	4	0.0012	16	15	11	-0.5	500	4(c), 5(e)-(f)
9	4	0.0012	16	15	11	-0.5	3600	8(c), 9(e)-(f)
10	4	0.0012	16	15	15	-0.5	1800	11

and frequency of a single soliton, propagating in an ultralong optical fiber, the situation can be very different for multiple soliton sequences, circulating in a fiber loop. In the latter case, Kerr-induced effects might lead to radiation emission, modulation instability, and eventually to pulse-pattern corruption [17]. It is therefore important to first analyze the effects of Kerr nonlinearity alone on the propagation. For this purpose, we carry out numerical simulations with the following coupled-NLS model, which incorporates second-order dispersion and Kerr nonlinearity, but neglects delayed Raman response and linear gain-loss:

$$i\partial_z\psi_j + \partial_t^2\psi_j + 2|\psi_j|^2\psi_j + 4\sum_{k=1}^{N}(1-\delta_{jk})|\psi_k|^2\psi_j = 0, \qquad (9)$$

where $1 \leq j \leq N$. The simulations are carried out for two, three, and four frequency channels with the physical parameter values listed in rows 2, 4, and 7 of Table 1. As an example, we present the results of the simulations for the following sets of initial soliton amplitudes: $\eta_1(0) = 0.9$, $\eta_2(0) = 1.05$ for $N = 2$; $\eta_1(0) = 0.9$, $\eta_2(0) = 0.95$, $\eta_3(0) = 1.1$ for $N = 3$; and $\eta_1(0) = 0.9$, $\eta_2(0) = 0.95$, $\eta_3(0) = 1.05$, $\eta_4(0) = 1.15$ for $N = 4$. We emphasize, however, that similar

Table 2: The dimensional parameters

№	N	τ_0 (ps)	$\tilde{T}$ (ps)	$\tilde{W}$ (THz)	X_s (km)	Figures
1	2	5	80	0.32	11875	1, 4(a), 5(a)-(b)
2	2	5	80	0	6875	2(a)-(b)
3	2	5	80	0.32	140000	8(a), 9(a)-(b)
4	3	5	80	0	6375	2(c)-(d)
5	3	5	80	0.32	7750	4(b), 5(c)-(d)
6	3	5	80	0.32	150625	8(b), 9(c)-(d)
7	4	5	80	0	4250	2(e)-(f)
8	4	5	80	0.35	6250	4(c), 5(e)-(f)
9	4	5	80	0.35	45000	8(c), 9(e)-(f)
10	4	5	80	0.48	22500	11

results are obtained with other choices of the initial soliton amplitudes. The numerical simulations are carried out up to a distance z_s, at which instability appears. More specifically, we define z_s as the largest distance at which the values of the integrals $I_j(z)$ in Eq. (A.3) in Appendix A are still smaller than 0.05 for $1 \le j \le N$. The actual value of z_s depends on the values of the physical parameters and in particular on the number of channels N. For the coupled-NLS simulations with Eq. (9) and the aforementioned initial amplitude values, we find $z_{s_1} = 550$ for $N = 2$, $z_{s_2} = 510$ for $N = 3$, and $z_{s_3} = 340$ for $N = 4$. Figure 2 shows the pulse patterns $|\psi_j(t, z_s)|$ and their Fourier transforms $|\hat{\psi}_j(\omega, z_s)|$ at the onset of instability, as obtained by the numerical solution of Eq. (9). Also shown are the theoretical predictions for the pulse patterns and their Fourier transforms at the onset of instability. Figure 3 shows magnified versions of the graphs in Fig. 2 for small $|\psi_j(t, z_s)|$ and $|\hat{\psi}_j(\omega, z_s)|$ values. The theoretical prediction for $|\psi_j(t, z_s)|$ is obtained by summation over fundamental NLS solitons with amplitudes $\eta_j(0)$, frequencies $\beta_j(0)$, and positions $y_j(z_s) + kT$ for $-J \le k \le J - 1$, which are measured from the simulations (see Appendix

A). The theoretical prediction for $|\hat{\psi}_j(\omega, z_s)|$ is obtained by taking the Fourier transform of the latter sum. As can be seen from Fig. 2, the soliton patterns are almost intact at $z = z_s$ for $N = 2, 3, 4$. Additionally, the soliton amplitude and frequency values are very close to their initial values. Thus, the solitons propagate in a stable manner up to the distance z_s. However, an examination of Figs. 3(a), 3(c), and 3(e) reveals that the soliton patterns are in fact slightly distorted at z_s, and that the distortion appears as fast oscillations in the solitons tails. Furthermore, as seen in Figs. 3(b), 3(d), and 3(f), the distortion is caused by resonant generation of radiaitive sidebands, where the largest sidebands for the jth soliton sequence form at frequencies $\beta_{j-1}(0)$ and/or $\beta_{j+1}(0)$ of the neighboring soliton sequences. In addition, the amplitudes of the radiative sidebands increase as the number of channels increases (see also Ref. [17] for similar behavior), and as a result, the stable propagation distance z_s decreases with increasing N. The growth of radiative sidebands and pulse distortion with increasing z eventually leads to the destruction of the soliton sequences. We point out that when each soliton sequence propagates through the fiber on its own, no radiative sidebands develop and no instability is observed up to distances as large as $z = 20000$ [17]. The latter finding is also in accordance with results of single-channel soliton transmission experiments, which demonstrated stable soliton propagation over distances as large as 10^6 km [60]. Based on these observations we conclude that transmission instability in the multichannel optical fiber system is caused by the Kerr-induced interaction in interchannel soliton collisions, that is, it is associated with the terms $2|\psi_k|^2\psi_j$ in Eq. (1).

We now take into account the effects of delayed Raman response and frequency dependent linear gain-loss on the propagation. Our first objective is to check the validity of the predator-prey model's predictions for collision-induced dynamics of soiton amplitudes in the presence of delayed Raman response. For this purpose, we carry out numerical simulations with the full coupled-NLS model (1) with the linear gain-loss function (2) for two, three, and four frequency channels with the physical parameter values listed in rows 1, 5, and 8 of Table 1. To enable comparison with the results presented in Figs. 2 and 3, we
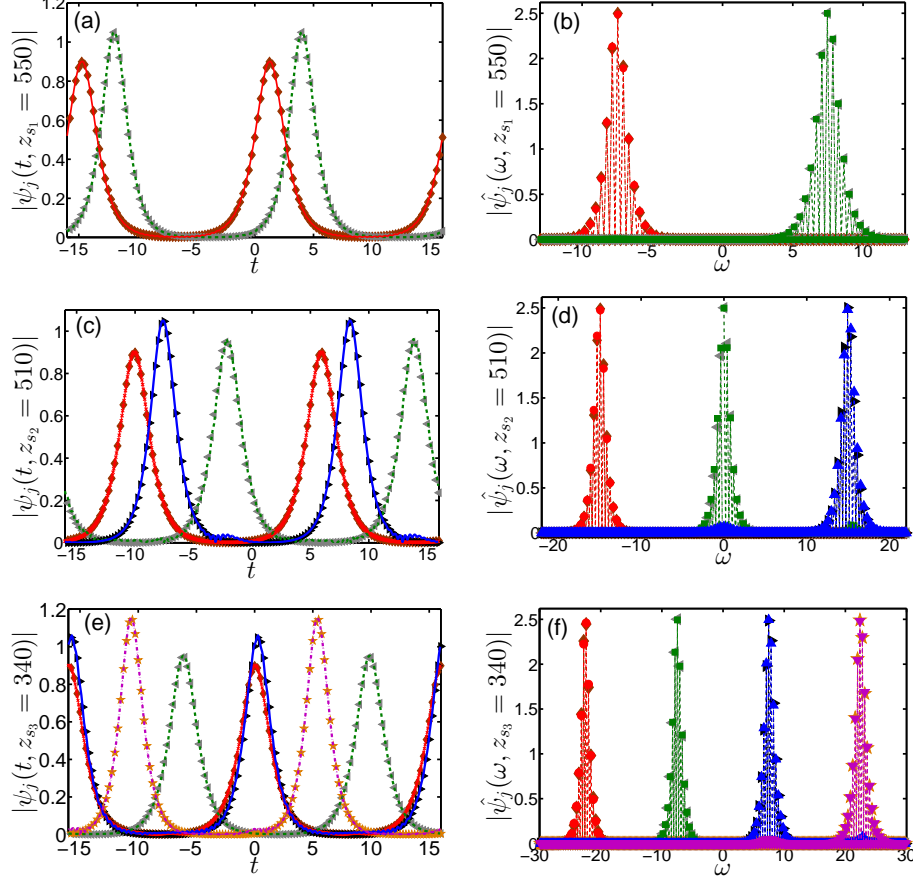
Figure 2: (Color online) The pulse patterns at the onset of transmission instability $|\psi_j(t, z_s)|$ and their Fourier transforms $|\hat{\psi}_j(\omega, z_s)|$ for two-channel [(a)-(b)], three-channel [(c)-(d)], and four-channel [(e)-(f)] transmission in the absence of delayed Raman response and linear gain-loss. The physical parameter values are listed in rows 2, 4, and 7 of Table 1. The stable transmission distances are $z_{s_1} = 550$ for $N = 2$, $z_{s_2} = 510$ for $N = 3$, and $z_{s_3} = 340$ for $N = 4$. The solid-crossed red curve [solid red curve in (a)], dashed green curve, solid blue curve, and dashed-dotted magenta curve represent $|\psi_j(t, z_s)|$ with $j = 1, 2, 3, 4$, obtained by numerical simulations with Eq. (9). The red circles, green squares, blue up-pointing triangles, and magenta down-pointing triangles represent $|\hat{\psi}_j(t, z_s)|$ with $j = 1, 2, 3, 4$, obtained by the simulations. The brown diamonds, gray left-pointing triangles, black right-pointing triangles, and orange stars represent the theoretical prediction for $|\psi_j(t, z_s)|$ or $|\hat{\psi}_j(\omega, z_s)|$ with $j = 1, 2, 3, 4$, respectively.
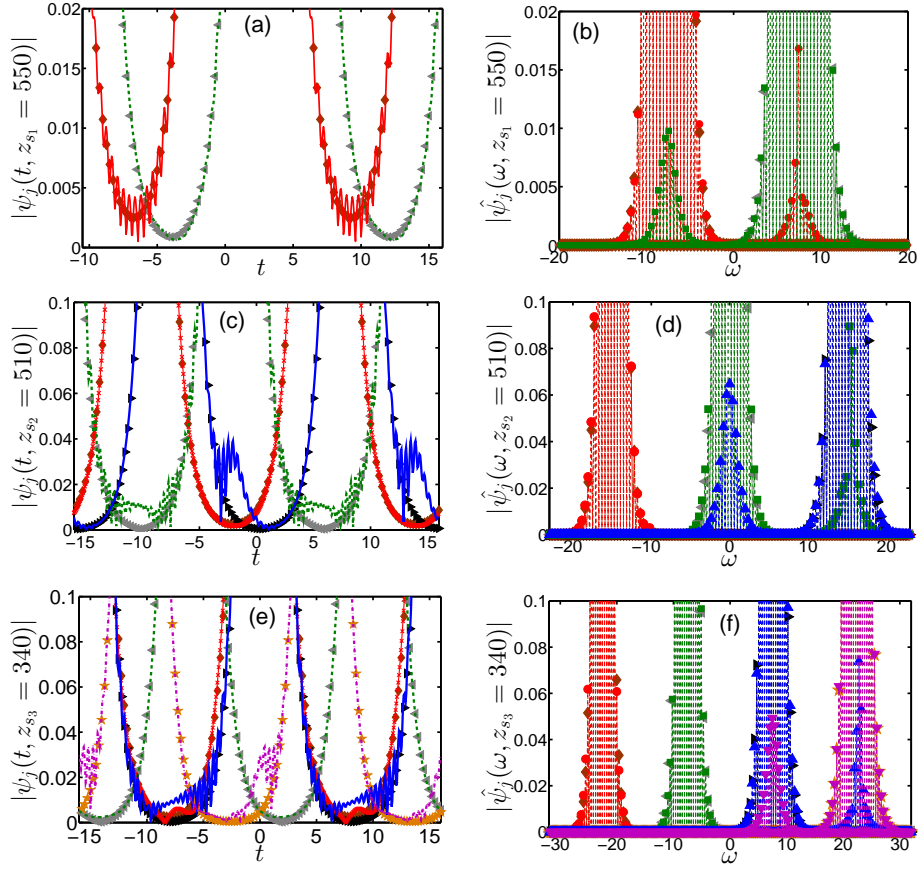
18

Figure 3: (Color online) Magnified versions of the graphs in Fig. 2 for small $|\psi_j(t, z_s)|$ and $|\hat{\psi}_j(\omega, z_s)|$ values. The symbols are the same as in Fig. 2.

19

discuss the results of simulations with the same sets of initial soliton amplitudes as the ones used in Figs. 2 and 3. The numerical simulations are carried out up to the onset of transmission instability, which occurs at $z_{s_4} = 950$ for $N = 2$, at $z_{s_5} = 620$ for $N = 3$, and at $z_{s_6} = 500$ for $N = 4$. The z dependence of soliton amplitudes obtained by numerical solution of the full coupled-NLS model (1) with the gain-loss (2) is shown in Fig. 4 along with the prediction of the predator-prey model (5). In all three cases the soliton amplitudes oscillate about their equilibrium value $\eta = 1$, i.e., the dynamics of soliton amplitudes is stable up to the distance z_s. Furthermore, the agreement between the coupled-NLS simulations and the predator-prey model's predictions is excellent throughout the propagation. Thus, our coupled-NLS simulations validate the predictions of the predator-prey model (5) for collision-induced amplitude dynamics in the presence of delayed Raman response at distances $0 \le z \le z_s$. This is a very important observation, because of the major simplifying assumptions that were made in the derivation of the model (5). In particular, we conclude that the effects of radiation emission, modulation instability, intrachannel interaction, and other high-order perturbations can indeed be neglected for distances smaller than z_s.

Further insight about transmission stability and about the processes leading to transmission destabilization is gained by an analysis of the soliton patterns at the onset of instability. Figure 5 shows the pulse patterns at the onset of instability $|\psi_j(t, z_s)|$ and their Fourier transforms $|\hat{\psi}_j(\omega, z_s)|$, obtained by the numerical simulations that are described in the preceding paragraph. The theoretical predictions for the pulse patterns and their Fourier transforms, which are calculated in the same manner as in Fig. 2, are also shown. In addition, Fig. 6 shows magnified versions of the graphs in Fig. 5 for small $|\psi_j(t, z_s)|$ and $|\hat{\psi}_j(\omega, z_s)|$ values. We observe that the soliton patterns are almost intact at z_s. Based on this observation and the observation that dynamics of soliton amplitudes is stable for $0 \le z \le z_s$ we conclude that the multichannel soliton-based transmission is stable at distances smaller than z_s. However, as seen in Figs. 6(a), 6(c), and 6(e), the soliton patterns are actually slightly distorted at z_s,
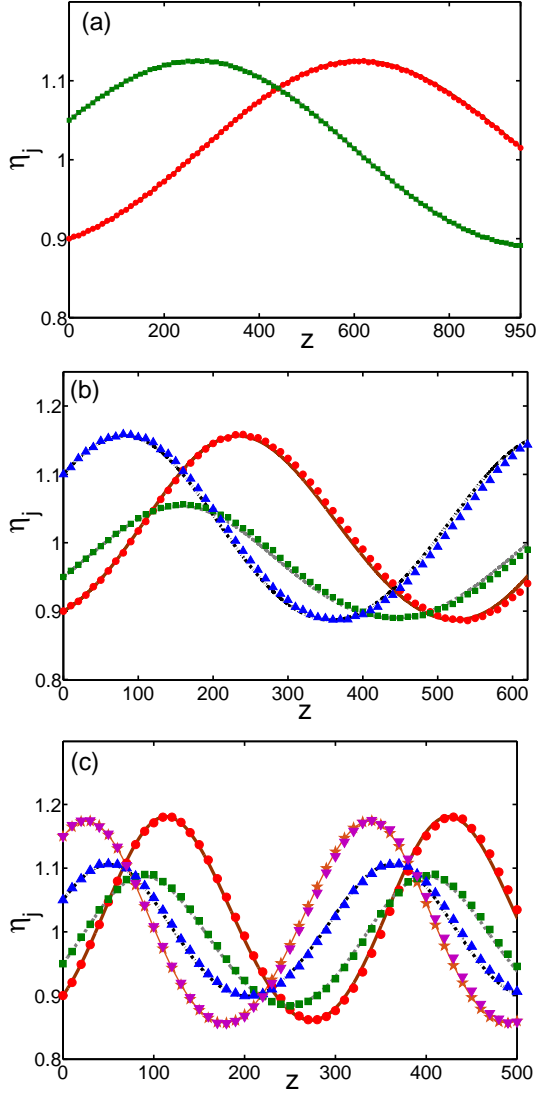
Figure 4: (Color online) The z dependence of soliton amplitudes η_j for two-channel (a), three-channel (b), and four-channel (c) transmission in the presence of delayed Raman response and the frequency dependent linear gain-loss (2). The physical parameter values are listed in rows 1, 5, and 8 of Table 1. The red circles, green squares, blue up-pointing triangles, and magenta down-pointing triangles represent $\eta_1(z)$, $\eta_2(z)$, $\eta_3(z)$, and $\eta_4(z)$, obtained by numerical solution of Eqs. (1) and (2). The solid brown, dashed gray, dashed-dotted black, and solid-starred orange curves correspond to $\eta_1(z)$, $\eta_2(z)$, $\eta_3(z)$, and $\eta_4(z)$, obtained by the predator-prey model (5).

21

and the distortion appears as fast oscillations in the solitons tails. Moreover, as seen in Figs. 6(b), 6(d), and 6(f), pulse-pattern distortion is caused by resonant formation of radiative sidebands, where the largest sidebands for the jth sequence form near the frequencies $\beta_{j-1}(z)$ and/or $\beta_{j+1}(z)$ of the neighboring soliton sequences. Thus, the mechanisms leading to deterioration of the soliton sequences in multichannel transmission in a single fiber in the presence of delayed Raman response and linear gain-loss are very similar to the ones observed in the absence of delayed Raman response and linear gain-loss. This also indicates that the dominant cause for transmission destabilization in the full coupled-NLS simulations for multichannel transmission in a single fiber is due to the effects of Kerr-induced interaction in interchannel soliton collisions. As explained earlier, the latter effects are represented by the $2|\psi_k|^2\psi_j$ terms in Eq. (1).

It is interesting to note that the stable propagation distances z_s in the presence of delayed Raman response and linear gain-loss are larger compared with the distances obtained in the absence of these two processes by factors of 1.7 for $N = 2$, 1.2 for $N = 3$, and 1.5 for $N = 4$. We attribute this moderate increase in z_s values to the introduction of frequency dependent linear gain-loss with strong loss g_L outside the frequency intervals $\beta_j(0) - W/2 < \omega \leq \beta_j(0) + W/2$, where $1 \leq j \leq N$, which leads to partial suppression of radiative sideband generation. However, the suppression of radiative instability in a single fiber is quite limited, since the radiative sidebands for a given sequence form near the frequencies $\beta_k(z)$ of the other soliton sequences. As a result, in a single fiber, one cannot employ strong loss at the latter frequencies, as this would lead to the decay of the propagating solitons. Better suppression of radiative instability and significantly larger z_s values can be realized in nonlinear waveguide couplers with frequency dependent linear gain-loss. This subject is discussed in detail in Section 4.

We now turn to discuss the later stages of pulse pattern deterioration, i.e., the evolution of the soliton sequences in a single fiber for distances $z > z_s$. As a concrete example, we discuss the four-channel setup considered in Figs. 4(c),
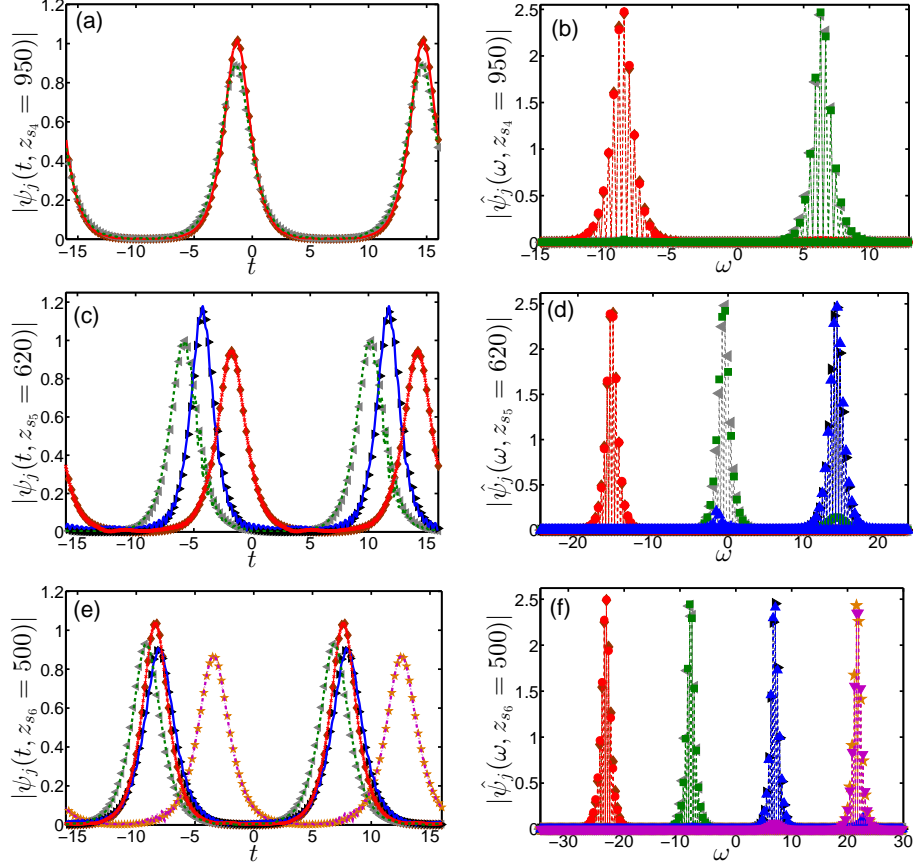
22

Figure 5: (Color online) The pulse patterns at the onset of transmission instability $|\psi_j(t, z_s)|$ and their Fourier transforms $|\hat{\psi}_j(\omega, z_s)|$ for two-channel [(a)-(b)], three-channel [(c)-(d)], and four-channel [(e)-(f)] transmission in the presence of delayed Raman response and the linear gain-loss (2). The physical parameter values are listed in rows 1, 5, and 8 of Table 1. The stable transmission distances are $z_{s_4} = 950$ for $N = 2$, $z_{s_5} = 620$ for $N = 3$, and $z_{s_6} = 500$ for $N = 4$. The solid-crossed red curve [solid red curve in (a)], dashed green curve, solid blue curve, and dashed-dotted magenta curve represent $|\psi_j(t, z_s)|$ with $j = 1, 2, 3, 4$, obtained by numerical simulations with Eqs. (1) and (2). The red circles, green squares, blue up-pointing triangles, and magenta down-pointing triangles represent $|\hat{\psi}_j(t, z_s)|$ with $j = 1, 2, 3, 4$, obtained by the simulations. The brown diamonds, gray left-pointing triangles, black right-pointing triangles, and orange stars represent the theoretical prediction for $|\psi_j(t, z_s)|$ or $|\hat{\psi}_j(\omega, z_s)|$ with $j = 1, 2, 3, 4$, respectively.
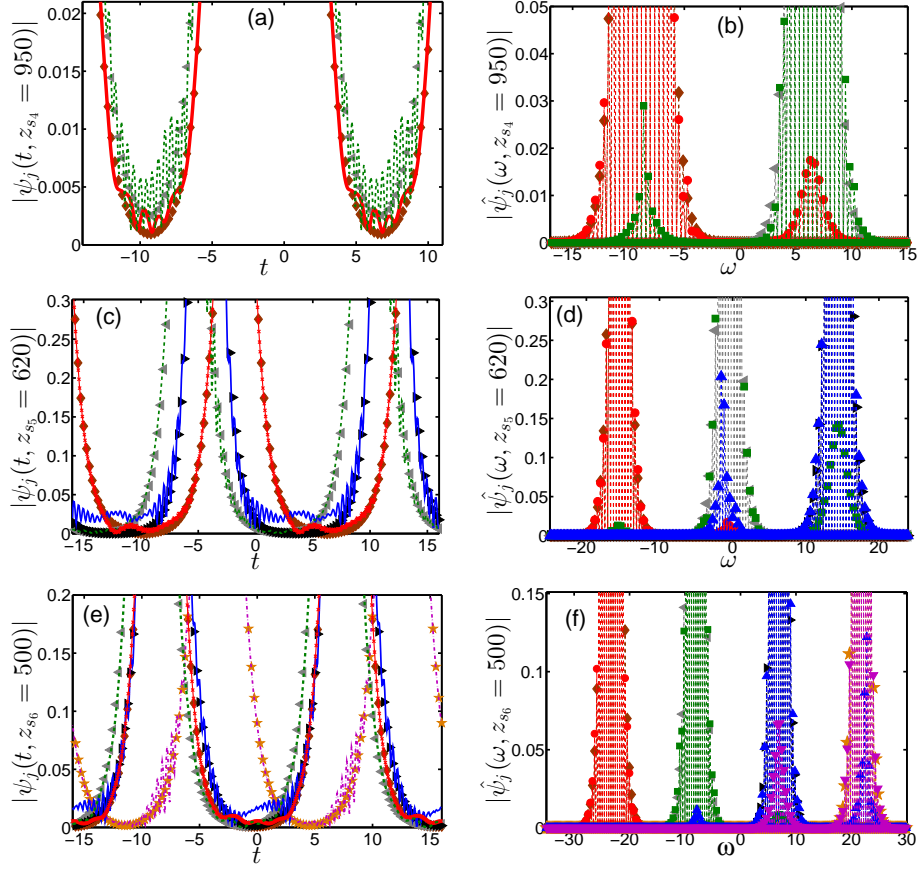
23

Figure 6: (Color online) Magnified versions of the graphs in Fig. 5 for small $|\psi_j(t, z_s)|$ and $|\hat{\psi}_j(\omega, z_s)|$ values. The symbols are the same as in Fig. 5.

24

5(e), and 5(f), for which $z_{s_6} = 500$ [59]. Figures 7(a) and 7(b) show the pulse patterns $|\psi_j(t, z)|$ and their Fourier transforms $|\hat{\psi}_j(\omega, z)|$ at $z = 600 > z_{s_6}$, as obtained by numerical solution of Eqs. (1) and (2). It is seen that the largest sidebands at $z = 600$ form near the frequency $\beta_3(z)$ for the $j = 2$ and $j = 4$ soliton sequences, and near the frequencies $\beta_2(z)$ and $\beta_4(z)$ for the $j = 3$ soliton sequence. These larger sidebands lead to significantly stronger pulse distortion at $z = 600$ compared with $z_{s_6} = 500$. In particular, at $z = 600$, the $j = 3$ pulse sequence is strongly distorted, where the distortion is in the form of fast oscillations in the main body of the solitons. In contrast, at $z_{s_6} = 500$, the $j = 3$ sequence is only weakly distorted, and the distortion is in the form of fast oscillations, which are significant only in the solitons tails. Additionally, radiation emitted by the solitons in the $j = 2$, $j = 3$, and $j = 4$ frequency channels develops into small pulses at $z = 600$. The largest radiation-induced pulses are generated due to radiation emitted by solitons in the $j = 4$ channel near the frequency $\beta_3(z)$. Figures 7(c) and 7(d) show a comparison of the shape and Fourier transform of the latter pulses with the shape and Fourier transform expected for a single NLS soliton with the same amplitude and frequency. It is clear that these radiation-induced pulses do not posses the soliton form. Similar conclusion holds for the other radiation-induced pulses. The amplitudes of the radiative sidebands generated by the $j = 2$, $j = 3$, and $j = 4$ pulse sequences continue to increase with increasing propagation distance and this leads to further pulse pattern degradation. Indeed, as seen in Fig. 7(f), at $z = 650$, the radiative sidebands generated by the $j = 4$ sequence near $\beta_3(z)$ and by the $j = 3$ sequence near $\beta_4(z)$ are comparable in magnitude to the Fourier transforms of the $j = 3$ and $j = 4$ pulse sequences, respectively. Additional strong radiative sidebands are observed for the $j = 2$ sequence near frequencies $\beta_3(z)$ and $\beta_4(z)$ and for the $j = 4$ sequence near frequency $\beta_2(z)$. As a result, the $j = 2$, $j = 3$, and $j = 4$ pulse sequences are strongly degraded due to pulse distortion at $z = 650$. More specifically, distortion due to fast oscillations in both the main body and the tail of the pulses is observed for these three pulse sequences [see Fig. 7(e)]. In addition, the number and amplitudes of

25

the radiation-induced pulses are much larger at $z = 650$ compared with the corresponding number and amplitudes of these pulses at $z = 600$.

4. Nonlinear waveguide coupler transmission

The results of the numerical simulations in Section 3 show that in a single fiber, radiative instabilities can be partially mitigated by employing the frequency dependent linear gain-loss (2). However, as described in Section 3, suppression of radiation emission in a single fiber is still quite limited, and generation of radiative sidebands leads to severe pulse pattern degradation at large distances. The limitation of the single-fiber setup is explained by noting that the radiative sidebands for each pulse sequence form near the frequencies $\beta_k(z)$ of the other pulse sequences. As a result, in a single fiber, one cannot employ strong loss at or near the frequencies $\beta_k(z)$, as this would lead to the decay of the propagating pulses. It is therefore interesting to look for other waveguide setups that can significantly enhance transmission stability. A very promising approach for enhancing transmission stability is based on employing a nonlinear waveguide coupler, consisting of N very close waveguides [17]. In this case each pulse sequence propagates through its own waveguide and each waveguide is characterized by its own frequency dependent linear gain-loss function $\tilde{g}_j(\omega, z)$ [61]. This enables better suppression of radiation emission, since the linear gain-loss of each waveguide can be set equal to the required g_j value within a certain z-dependent bandwidth $(\beta_j(z)-W/2, \beta_j(z)+W/2]$ around the central frequency $\beta_j(z)$ of the solitons in that waveguide, and equal to a relatively large negative value g_L outside of that bandwidth. This leads to enhancement of transmission stability compared with the single fiber setup, since generation of all radiative sidebands outside of the interval $(\beta_j(z) - W/2, \beta_j(z) + W/2]$ is suppressed by the relatively strong linear loss g_L.

In the current section, we investigate the possibility to significantly enhance transmission stability in multichannel soliton-based systems by employing N-waveguide couplers with frequency dependent linear gain-loss. The enhanced
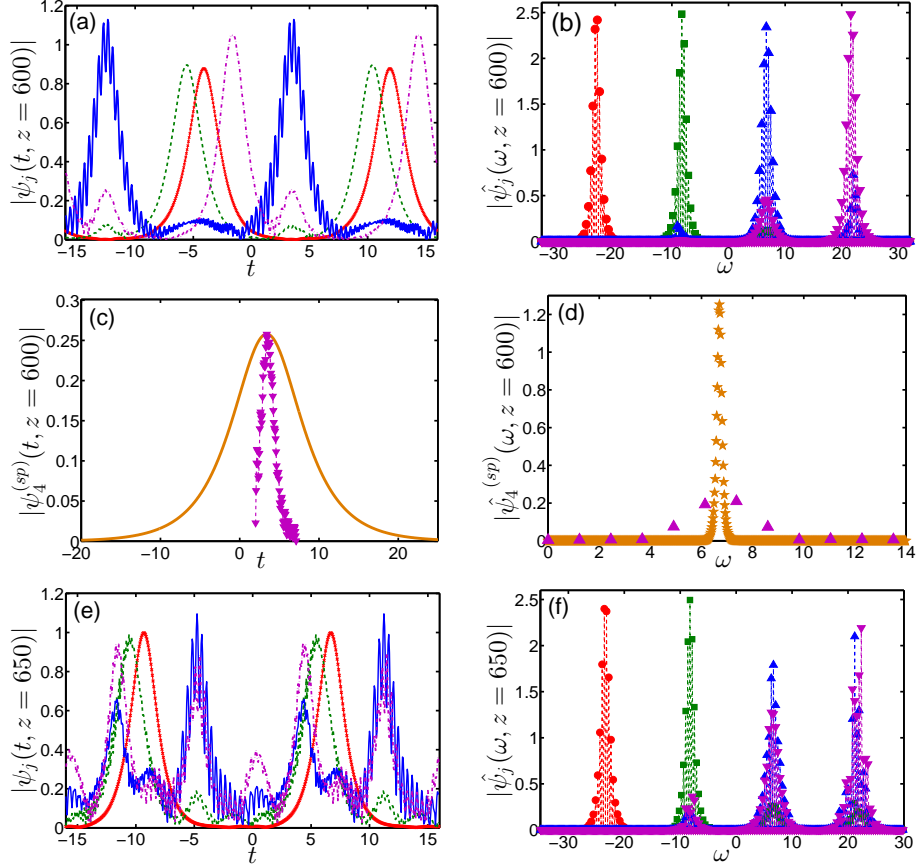
26

Figure 7: (Color online) The pulse patterns $|\psi_j(t,z)|$ and their Fourier transforms $|\hat{\psi}_j(\omega,z)|$ at $z=600$ [(a) and (b)] and at $z=650$ [(e) and (f)], obtained by numerical simulations with Eqs. (1) and (2) for the four-channel system considered in Figs. 4 and 5. The symbols in (a), (b), (e), and (f) are the same as in Fig. 5. (c) The shape of a radiation-induced pulse $|\psi_4^{(sp)}(t,z)|$, generated due to radiation emitted by the $j=4$ soliton sequence at $z=600$. The magenta down-pointing triangles represent the numerically obtained $|\psi_4^{(sp)}(t,z)|$ with $z=600$, while the solid orange curve corresponds to the shape of a single NLS soliton with the same amplitude. (d) The Fourier transform of the radiation-induced pulse in (c). The magenta down-pointing triangles represent the numerically obtained $|\hat{\psi}_4^{(sp)}(\omega,z)|$ with $z=600$, while the solid orange curve corresponds to the Fourier transform of a single NLS soliton with the same amplitude and central frequency.

27

transmission stability is also expected to enable observation of the stable oscillatory dynamics of soliton amplitudes, predicted by the predator-prey model (5), along significantly larger distances compared with the distances observed in single-fiber transmission. Similar to the single-fiber setup considered in Section 3, we take into account the effects of second-order dispersion, Kerr nonlinearity, delyaed Raman response, and linear gain-loss. The main difference between the waveguide coupler setup and the single-fiber setup is that the single linear gain-loss function $\tilde{g}(\omega)$ of Eq. (2) is now replaced by N z-dependent linear gain-loss functions $\tilde{g}_j(\omega, z)$, where $1 \leq j \leq N$. Thus, the propagation of the pulse sequences through the waveguide coupler is described by the following coupled-NLS model:

$$i\partial_z\psi_j + \partial_t^2\psi_j + 2|\psi_j|^2\psi_j + 4\sum_{k=1}^{N}(1 - \delta_{jk})|\psi_k|^2\psi_j = i\mathcal{F}^{-1}(\tilde{g}_j(\omega, z)\hat{\psi}_j)/2$$

$$-\epsilon_R\psi_j\partial_t|\psi_j|^2 - \epsilon_R\sum_{k=1}^{N}(1 - \delta_{jk})\left[\psi_j\partial_t|\psi_k|^2 + \psi_k\partial_t(\psi_j\psi_k^*)\right], \tag{10}$$

where $1 \leq j \leq N$. The linear gain-loss function of the jth waveguide $\tilde{g}_j(\omega, z)$, appearing on the right-hand side of Eq. (10), is defined by:

$$\tilde{g}_j(\omega, z) = \begin{cases} g_j & \text{if } \beta_j(z) - W/2 < \omega \leq \beta_j(z) + W/2, \\ g_L & \text{if } \omega \leq \beta_j(z) - W/2, \text{ or } \omega > \beta_j(z) + W/2, \end{cases} \tag{11}$$

where the g_j coefficients are determined by Eq. (4), the z dependence of the frequencies $\beta_j(z)$ is determined from the numerical solution of the coupled-NLS model (10), and $g_L < 0$. Notice the following important properties of the gain-loss (11). First, the gain-loss g_j inside the central frequency interval $(\beta_j(z) - W/2, \beta_j(z) + W/2]$ is expected to compensate for amplitude shifts due to Raman crosstalk and by this, lead to stable oscillatory dynamics of soliton amplitudes. Second, the relatively strong linear loss g_L outside the interval $(\beta_j(z) - W/2, \beta_j(z) + W/2]$ should enable efficient suppression of radiative sideband generation for *any frequency* outside of this interval. Third, the end points of the central frequency interval are shifting with z, such that the interval is centered around $\beta_j(z)$ throughout the propagation. This shifting of the central

28

amplification interval is introduced to compensate for the significant Raman-induced frequency shifts experienced by the solitons during the propagation [62]. The combination of the three properties of $\tilde{g}_j(\omega, z)$ should lead to a significant increase of the stable transmission distances in the nonlinear N-waveguide coupler compared with the single-fiber system considered in Section 3. As a result, one can expect that the stable oscillatory dynamics of soliton amplitudes, predicted by the predator-prey model (5), will also hold along significantly larger distances.

In order to check whether the N-waveguide coupler setup leads to enhancement of transmission stability, we numerically solve Eq. (10) with the gain-loss (11) for two, three, and four channels. The comparison with results obtained for single-fiber transmission is enabled by using the same values of the physical parameters that were used in Figs. 4(a), 4(b) and 4(c). The numerical simulations are carried out up to the onset of transmission instability, which occurs at $z_{s_7} = 11200$ for $N = 2$, $z_{s_8} = 12050$ for $N = 3$, and $z_{s_9} = 3600$ for $N = 4$. Figure 8 shows the z dependence of soliton amplitudes as obtained by the coupled-NLS simulations along with the prediction of the predator-prey model (5). It is seen that the amplitudes exhibit stable oscillations about the equilibrium value $\eta = 1$ for $N = 2, 3$, and 4. Furthermore, the agreement between the coupled-NLS simulations and the predictions of the predator-prey model are excellent throughout the propagation. Thus, both transmission stability and the validity of the predator-prey model's predictions are extended to distances that are larger by factors of 11.8 for $N = 2$, 19.4 for $N = 3$, and 7.2 for $N = 4$ compared with the distances obtained with the single-fiber WDM system in Section 3.

Further insight into the enhanced transmission stability in waveguide couplers is gained by analyzing the pulse patterns at the onset of instability $|\psi_j(t, z_s)|$ and their Fourier transforms $|\hat{\psi}_j(\omega, z_s)|$. Figure 9 shows the results obtained by numerical solution of Eqs. (10) and (11) together with the theoretical prediction. Figure 10 shows magnified versions of the graphs in Fig. 9 for small $|\psi_j(t, z_s)|$ and $|\hat{\psi}_j(\omega, z_s)|$ values. It is seen that the soliton patterns are almost
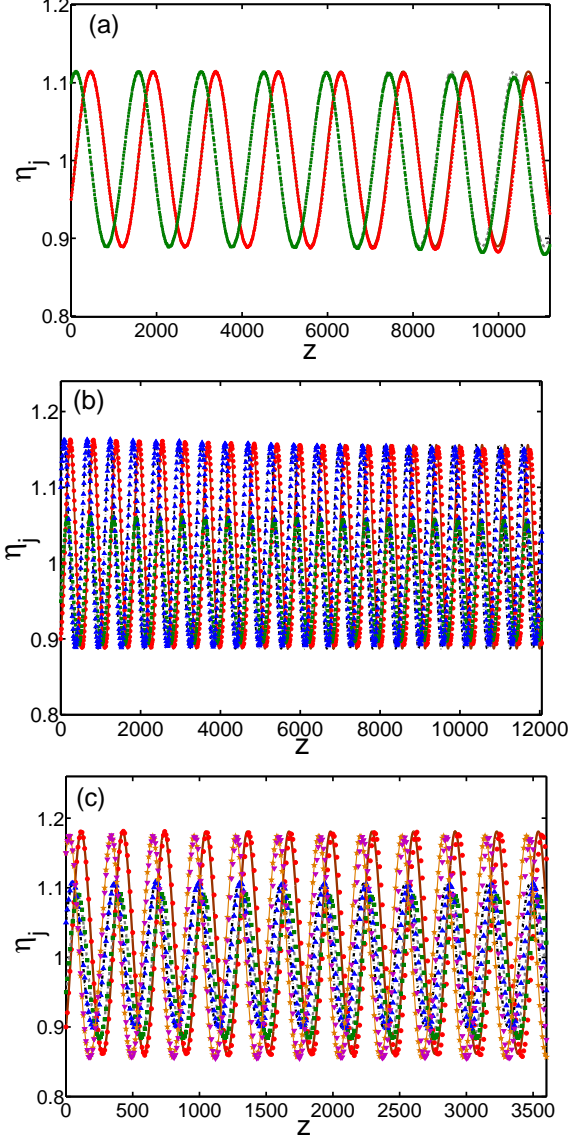
29

Figure 8: (Color online) The z dependence of soliton amplitudes η_j in a two-channel (a), a three-channel (b), and a four-channel (c) nonlinear waveguide coupler with linear gain-loss (11). The values of the physical parameters are the same as the ones used in Fig. 4. The red circles, green squares, blue up-pointing triangles, and magenta down-pointing triangles represent $\eta_1(z)$, $\eta_2(z)$, $\eta_3(z)$, and $\eta_4(z)$ obtained by numerical solution of the coupled-NLS model (10) with the gain-loss (11). The solid brown, dashed gray, dashed-dotted black, and solid-starred orange curves correspond to $\eta_1(z)$, $\eta_2(z)$, $\eta_3(z)$, and $\eta_4(z)$ obtained by the predator-prey model (5).

intact at $z = z_s$, in accordance with our conclusion about transmission stability for $0 \leq z \leq z_s$. Moreover, as seen from Fig. 10, no radiative sidebands and no fast oscillations in the solitons shapes are observed at $z = z_s$. Instead, soliton distortion at $z = z_s$ is due to slow variations in the shape at the pulse tails, formation of small radiative pulses, and position shifts of the solitons from the same sequence relative to one another. Thus, instability due to formation of radiative sidebands is completely suppressed in N-waveguide couplers with the gain-loss (11). This finding explains the significant increase in the values of the stable propagation distance in N-waveguide coupler transmission compared with the distances achieved in single-fiber transmission in Section 3.

We note that the frequency shifts experienced by the propagating solitons at large propagation distances are quite large for both the single-fiber systems of Section 3 and the N-waveguide coupler systems of the current section. For example, the total frequency shifts measured at $z_{s_9} = 3600$ from the coupled-NLS simulations for the four-channel waveguide coupler of Fig. 8(c) are $\Delta\beta_1(z_{s_9}) = -7.354$, $\Delta\beta_2(z_{s_9}) = -7.296$, $\Delta\beta_3(z_{s_9}) = -7.284$, and $\Delta\beta_4(z_{s_9}) = -7.2204$. These Raman-induced frequency shifts make the gain-loss functions with fixed frequency intervals [such as the function in Eq. (2)] less effective in stabilizing soliton amplitude dynamics. In order to compensate for the effects of these frequency shifts, a shifting of the central amplification interval was introduced into the gain-loss function (11). We now complete the analysis of transmission stabilization in the waveguide coupler, by evaluating the impact of shifting of the amplification interval in the gain-loss function (11). For this purpose, we consider the following alternative gain-loss functions with *fixed* amplification intervals:

$$\tilde{g}_j(\omega) = \begin{cases} g_j & \text{if } \beta_j(0) - W/2 < \omega \leq \beta_j(0) + W/2, \\ g_L & \text{if } \omega \leq \beta_j(0) - W/2, \text{ or } \omega > \beta_j(0) + W/2, \end{cases} \quad (12)$$

where $1 \leq j \leq N$. We carry out numerical simulations with Eq. (10) and the gain-loss functions (12) with $W = 15$ for a four-channel waveguide coupler. The values of the other physical parameters are the same as the ones used in Fig.
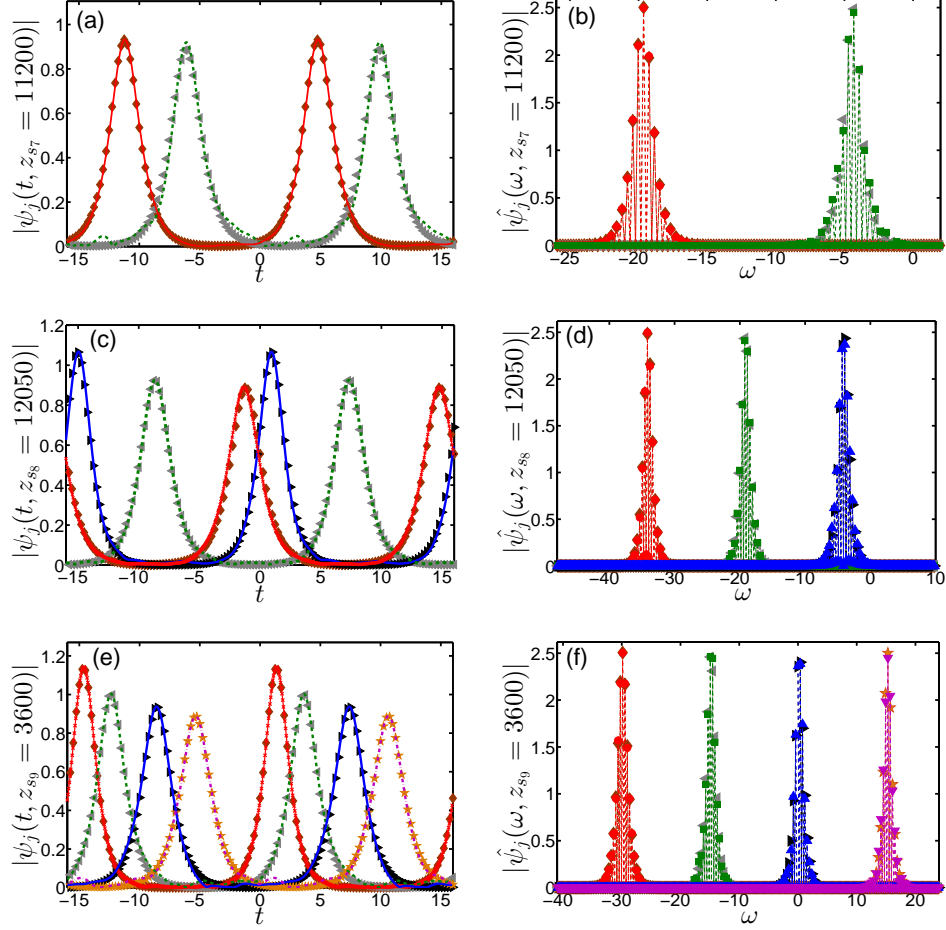
31

Figure 9: (Color online) The pulse patterns at the onset of instability $|\psi_j(t, z_s)|$ and their Fourier transforms $|\hat{\psi}_j(\omega, z_s)|$ for the two-channel [(a)-(b)], the three-channel [(c)-(d)], and the four-channel [(e)-(f)] waveguide couplers of Fig. 8. The final distances are $z_{s_7} = 11200$ in (a)-(b), $z_{s_8} = 12050$ in (c)-(d), and $z_{s_9} = 3600$ in (e)-(f). The solid-crossed red curve [solid red curve in (a)], dashed green curve, solid blue curve, and dashed-dotted magenta curve represent $|\psi_j(t, z_s)|$ with $j = 1, 2, 3, 4$, obtained by numerical simulations with Eqs. (10) and (11). The red circles, green squares, blue up-pointing triangles, and magenta down-pointing triangles represent $|\hat{\psi}_j(t, z_s)|$ with $j = 1, 2, 3, 4$, obtained by the simulations. The brown diamonds, gray left-pointing triangles, black right-pointing triangles, and orange stars represent the theoretical prediction for $|\psi_j(t, z_s)|$ or $|\hat{\psi}_j(\omega, z_s)|$ with $j = 1, 2, 3, 4$, respectively.
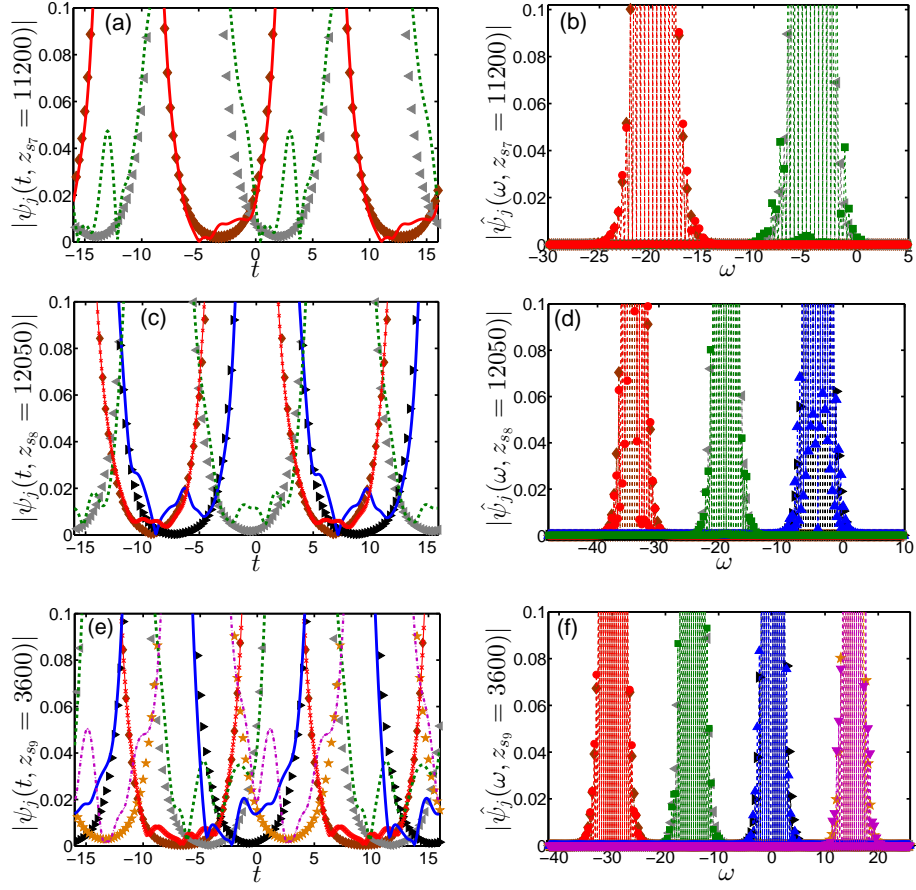
Figure 10: (Color online) Magnified versions of the graphs in Fig. 9 for small $|\psi_j(t, z_s)|$ and $|\hat{\psi}_j(\omega, z_s)|$ values. The symbols are the same as in Fig. 9.

8(c). The simulations are carried out up to the onset of transmisison instability at $z_{s_{10}} = 1800$. Figure 11 shows the z dependence of soliton amplitudes obtained by these coupled-NLS simulations along with the prediction of the predator-prey model (5). We observe stable oscillatory dynamics and good agreement with the predator-prey model's prediction throughout the propagation. We note that the stable propagation distance $z_{s_{10}} = 1800$ is larger by a factor of 3.6 compared with the stable propagation distance for the corresponding single-fiber system [see Fig. 4(c)], but smaller by a factor of 0.5 compared with the distance obtained with the waveguide coupler and the gain-loss (11). Based on this comparison we conclude that the introduction of shifting of the central amplification interval does lead to an enhancement of transmission stability. On the other hand, we also observe that even in the absence of shifting of the amplification interval, the waveguide coupler setup enables stable propagation along significantly larger distances compared with the single-fiber systems considered in Section 3.

We conclude this section by summarizing the dependence of the stable propagation distance z_s on the number of channels N in the main transmission setups considered in the paper. Figure 12 shows the z_s values obtained by numerical simulations for single-fiber transmission with and without the effects of delayed Raman response and the linear gain-loss (2). The z_s values obtained by the simulations for N-waveguide coupler transmission with the linear gain-loss (11) are also shown. We observe that in single-fiber transmission, the introduction of the gain-loss (2) leads to a moderate increase in the z_s values, despite of the presence of delayed Raman response. Moreover, the z_s values obtained in N-waveguide coupler transmission are significantly larger than the ones obtained in single-fiber transmission. As explained earlier, the enhanced transmission stability in waveguide couplers can be attributed to the more efficient suppression of radiative sideband generation by the linear gain-loss (11).
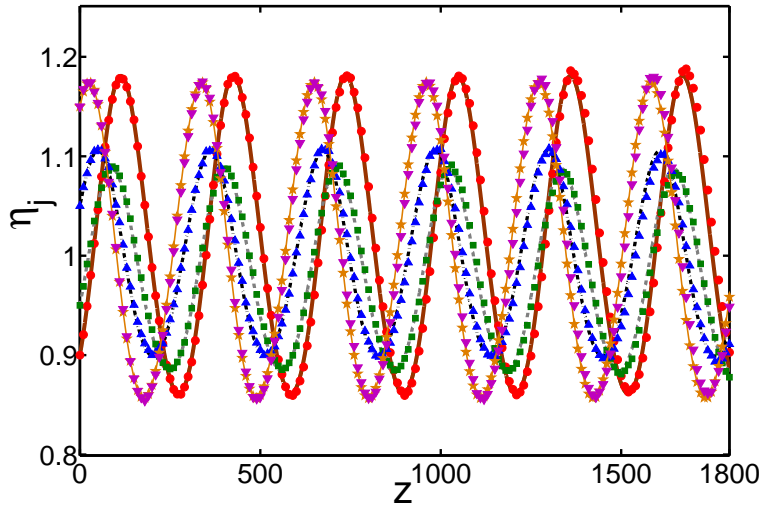
34

Figure 11: (Color online) The z dependence of soliton amplitudes η_j in a four-channel nonlinear waveguide coupler with linear gain-loss (12) and $W = 15$. The values of the other physical parameters are the same as the ones used in Fig. 8 (c). The red circles, green squares, blue up-pointing triangles, and magenta down-pointing triangles represent $\eta_1(z)$, $\eta_2(z)$, $\eta_3(z)$, and $\eta_4(z)$ obtained by numerical solution of the coupled-NLS model (10) with the gain-loss (12). The solid brown, dashed gray, dashed-dotted black, and solid-starred orange curves correspond to $\eta_1(z)$, $\eta_2(z)$, $\eta_3(z)$, and $\eta_4(z)$ obtained with the predator-prey model (5).
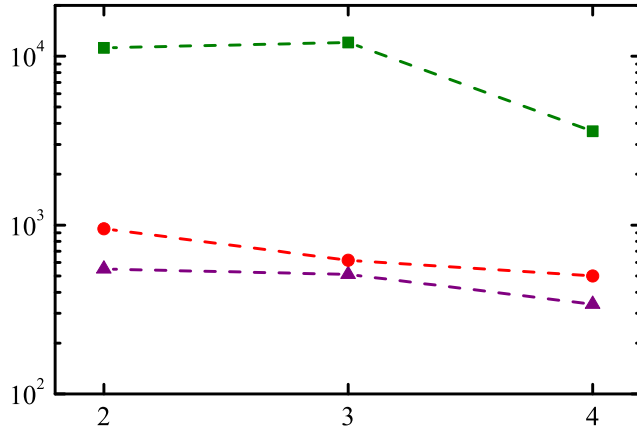
Figure 12: (Color online) The dependence of the stable propagation distance z_s on the number of channels N in different transmission setups. The red circles represent the values obtained for single-fiber transmission in the presence of delayed Raman response and the linear gain-loss (2) by numerical solution of Eqs. (1) and (2). The purple triangles represent the values obtained for single-fiber transmission in the absence of delayed Raman response and linear gain-loss by numerical solution of Eq. (9). The green squares represent the values obtained for N-waveguide coupler transmission by numerical solution of Eqs. (10) and (11).

5. Conclusions

We investigated transmission stabilization and destabilization and dynamics of pulse amplitudes induced by Raman crosstalk in multichannel soliton-based optical waveguide systems with N frequency channels. We considered two main transmission setups. In the first setup, the N soliton sequences propagate through a single optical fiber, while in the second setup, the sequences propagate through a waveguide coupler, consisting of N close waveguides. We studied the transmission by performing numerical simulations with coupled-NLS models, which take into account second-order dispersion, Kerr nonlinearity, delayed Raman response, and frequency dependent linear gain-loss. The simulations were carried out for two, three, and four frequency channels in both single-fiber and waveguide coupler setups. The results of the coupled-NLS simulations were compared with the predictions of a simplified predator-prey model for dynamics of pulse amplitudes [43], which incorporates amplitude shifts due to linear gain-loss and delayed Raman response, but neglects radiation emission and intrachannel interaction. The predator-prey model in Ref. [43] predicts that stable dynamics of soliton amplitudes can be realized by a suitable choice of amplifier gain in different frequency channels. One major goal of our study was to validate this prediction. A second major goal was to characterize the processes that lead to transmission destabilization and to develop waveguide setups, which lead to significant enhancement of transmission stability.

We first studied soliton-based multichannel transmission in a single fiber in the absence of delayed Raman response and linear gain-loss. We found that in this case, transmission destabilization is caused by resonant formation of radiative sidebands, where the largest sidebands for the jth soliton sequence form at frequencies $\beta_{j-1}(0)$ and / or $\beta_{j+1}(0)$ of the solitons in the neighboring frequency channels. Additionally, the amplitudes of the radiative sidebands increase with increasing number of channels N, and as a result, the stable propagation distances decrease with increasing N. Furthermore, the stable propagation distances obtained in our numerical simulations are significantly smaller compared

37

with the distances achieved in Ref. [17] for single-channel transmission with the same values of the physical parameters. Based on these findings we conclude that destabilization of multichannel soliton-based transmission in a single fiber is caused by Kerr-induced interaction in interchannel soliton collisions.

We then carried out numerical simulations for multichannel transmission in a single fiber, taking into account the effects of delayed Raman response and frequency dependent linear gain-loss. We assumed that the gain-loss function $g(\omega)$ for single-fiber transmission is given by Eq. (2). That is, $g(\omega)$ is equal to the constants g_j, determined by the predator-prey model, in frequency intervals $(\beta_j(0) - W/2, \beta_j(0) + W/2]$ of constant width W centered about the initial soliton frequencies $\beta_j(0)$, and is equal to a negative value g_L outside of these intervals. Numerical simulations with the full coupled-NLS model showed that at distances smaller than the stable propagation distance z_s, soliton amplitudes exhibit stable oscillatory dynamics, in excellent agreement with the predictions of the predator-prey model of Ref. [43]. These findings are very important because of the major simplifying assumptions made in the derivation of the predator-prey model. In particular, based on these findings, we conclude that the effects of radiation emission and intrachannel interaction can indeed be neglected at distances smaller than z_s. However, at distances $z \simeq z_s$, we observed transmission destabilization due to formation of radiative sidebands. The destabilization process is very similar to destabilization in the absence of delayed Raman response and linear gain-loss, i.e., the largest sidebands for the jth soliton sequence form at frequencies $\beta_{j-1}(z)$ and / or $\beta_{j+1}(z)$ of the solitons in the neighboring frequency channels. At distances larger than z_s, the continued growth of the radiative sidebands leads to fast oscillations in the main body of the solitons and to generation of new pulses, which do not possess the soliton sech form. As a result, the pulse patterns at this late stage of the propagation are strongly distorted.

We note that the stable propagation distances z_s for single-fiber multichannel transmission in the presence of delayed Raman response and linear gain-loss are larger compared with the distances obtained in the absence of these pro-

cess. We attribute this increase in z_s values to the introduction of frequency dependent linear gain-loss with relatively strong loss g_L outside the frequency intervals $(\beta_j(0) - W/2, \beta_j(0) + W/2]$, which leads to partial suppression of radiative sideband generation. However, the suppression of radiative instability in single-fiber transmission is quite limited, since the radiative sidebands for each sequence form near the frequencies $\beta_k(z)$ of the other soliton sequences. As a result, in a single fiber, one cannot employ strong loss at the latter frequencies, as this would lead to the decay of the propagating solitons.

A more promising approach for achieving significant enhancement of transmission stability is based on employing a nonlinear waveguide coupler, consisting of N close waveguides. In this case, each soliton sequence propagates through its own waveguide, and each waveguide is characterized by its own frequency dependent linear gain-loss function. We assumed that the linear gain-loss for the jth waveguide $\tilde{g}_j(\omega, z)$ is equal to the constant g_j, determined by the predator-prey model, inside a z-dependent frequency interval centered about the soliton frequency $\beta_j(z)$, and is equal to a negative value g_L outside of this interval. This waveguide coupler setup is expected to lead to enhanced transmission stability, since generation of all radiative sidebands outside of the central amplification interval is suppressed by the relatively strong linear loss g_L for each of the N waveguides. To test this prediction, we carried out numerical simulations with a new coupled-NLS model, which takes into account the effects of second-order dispersion, Kerr nonlinearity, delayed Raman response, and the N frequency-dependent linear gain-loss functions $\tilde{g}_j(\omega, z)$. The simulations with the new coupled-NLS model showed that transmission stability and the validity of the predator-prey model's predictions in waveguide coupler transmission are extended to distances that are larger by factors of 11.8 for two channels, 19.4 for three channels, and 7.2 for four channels, compared with the distances in the single-fiber system. Additionally, the simulations showed that the solitons retain their shape at distances smaller than z_s and no radiative sidebands appear throughout the propagation. Based on these observations we conclude that transmission stability in the waveguide coupler system is indeed

39

significantly enhanced compared with the single-fiber system. Furthermore, the enhanced transmission stability in the waveguide coupler is enabled by the efficient suppression of radiative sideband generation due to the presence of the linear gain-loss $\tilde{g}_j(\omega, z)$.

To complete the analysis of transmission stabilization in the waveguide coupler, we evaluated the impact of the shifting of the central amplification intervals of the gain-loss functions $\tilde{g}_j(\omega, z)$. For this purpose, we replaced each $\tilde{g}_j(\omega, z)$ by a z-independent gain-loss function $\tilde{g}_j(\omega)$ that is equal to g_j inside a *fixed* frequency interval centered about the initial soliton frequency $\beta_j(0)$, and is equal to a negative value g_L outside of this interval. Numerical simulations with the coupled-NLS model for a four-channel system showed that the stable propagation distance and the distance along which the predator-prey model's predictions are valid are larger by a factor of 3.6 compared with the distance achieved in the single-fiber system, but smaller by a factor of 0.5 compared with the distance obtained in the waveguide coupler with shifting of the central amplification intervals of the linear gain-loss. Based on these findings we conclude that the introduction of shifting of the central amplification intervals does lead to enhanced transmission stability. On the other hand, even in the absence of shifting of the central amplification intervals, the waveguide coupler setup enables stable propagation along significantly larger distances compared with the single-fiber setup.

Appendix A. The method for determining the stable propagation distance

In this Appendix, we present the method that we used for determining the value of the stable propagation distance z_s from the results of the coupled-NLS simulations. In addition, we present the theoretical predictions for the soliton patterns and their Fourier transforms, which were used in the analysis of transmission stability.

We consider propagation of the soliton sequence in the jth frequency channel

through an optical waveguide, where the envelope of the electric field of this sequence at $z = 0$ is given by Eq. (8). We are interested in the envelope of the pulse sequence at distance z. We assume that the pulse sequence is only weakly distorted at this distance. Thus, by the standard adiabatic perturbation technique for the NLS soliton, one can write the envelope of the electric field of the jth sequence at distance z as: $\psi_j(t, z) = \psi_{tj}(t, z) + v_{rj}(t, z)$, where $\psi_{tj}(t, z)$ is the soliton part and $v_{rj}(t, z)$ is the radiation part [63, 64]. Since $T \gg 1$, we neglect intrasequence interaction, in accordance with the assumptions of the predator-prey model of Ref. [43] (see also Section 2). Under this assumption, the soliton part of the electric field can be expressed as:

$$\psi_{tj}(t, z) = \eta_j(z) e^{i\theta_j(z)} \sum_{k=-J}^{J-1} \frac{\exp\{i\beta_j(z)\,[t - y_j(z) - kT]\}}{\cosh\{\eta_j(z)\,[t - y_j(z) - kT]\}}, \quad \text{(A.1)}$$

where $\eta_j(z)$ is the amplitude, $\beta_j(z)$ is the frequency, $\theta_j(z)$ is the common overall phase, $y_j(z) = \Delta y_j(z) + T/2 + \delta_j$, and $\Delta y_j(z)$ is the common overall position shift. The Fourier transform of $\psi_{tj}(t, z)$ with respect to time is given by:

$$\hat{\psi}_{tj}(\omega, z) = \left(\frac{\pi}{2}\right)^{1/2} \operatorname{sech}\left\{\frac{\pi\,[\omega - \beta_j(z)]}{2\eta_j(z)}\right\} e^{i\theta_j(z) - i\omega y_j(z)} \sum_{k=-J}^{J-1} e^{-ikT\omega}. \text{(A.2)}$$

Our theoretical prediction for the jth pulse pattern at distance z, $|\psi_j^{(th)}(t, z)|$, is calculated by using Eq. (A.1) with values of $\eta_j(z)$, $\beta_j(z)$, and $y_j(z)$, which are measured from the numerical simulations. Similarly, our theoretical prediction for the Fourier transform of the jth pulse pattern, $|\hat{\psi}_j^{(th)}(\omega, z)|$, is obtained by using Eq. (A.2) with the numerically obtained values of $\eta_j(z)$ and $\beta_j(z)$ [65].

The method for determining the stable propagation distance is based on a comparison of the theoretical predictions for the pulse patterns $|\psi_j^{(th)}(t, z)|$ with the results of the numerical simulation $|\psi_j^{(num)}(t, z)|$ for $1 \leq j \leq N$. More specifically, we calculate the following normalized integrals, which measure the deviation of the numerically obtained pulse patterns from the corresponding theoretical predictions:

$$I_j(z) = \tilde{I}_j^{(dif)}(z)/\tilde{I}_j(z), \quad \text{(A.3)}$$

where

$$\tilde{I}_j^{(dif)}(z) = \left\{ \int\limits_{-JT}^{JT} \left[\left| \psi_j^{(th)}(t,z) \right| - \left| \psi_j^{(num)}(t,z) \right| \right]^2 dt \right\}^{1/2}, \quad \text{(A.4)}$$

$$\tilde{I}_j(z) = \left[\int\limits_{-JT}^{JT} \left| \psi_j^{(th)}(t,z) \right|^2 dt \right]^{1/2}, \quad \text{(A.5)}$$

and $1 \leq j \leq N$. We then define the stable propagation distance z_s as the largest distance at which the values of $I_j(z)$ are still smaller than a constant C for $1 \leq j \leq N$. In practice, we used the value $C = 0.05$ in the numerical simulations. We emphasize, however, that the values of the stable propagation distance obtained by this method are not very sensitive to the choice of the constant C. That is, we found that small changes in the value of C lead to small changes in the measured z_s values.

References

References

[1] G.P. Agrawal, *Nonlinear Fiber Optics* (Academic, San Diego, CA, 2001).

[2] F. Forghieri, R.W. Tkach, and A.R. Chraplyvy, in *Optical Fiber Telecommunications III*, I.P. Kaminow and T.L. Koch, eds., (Academic, San Diego, CA, 1997), Chapter 8.

[3] L.F. Mollenauer and J.P. Gordon, *Solitons in Optical Fibers: Fundamentals and Applications* (Academic, San Diego, CA, 2006).

[4] A.H. Gnauck, R.W. Tkach, A.R. Chraplyvy, and T. Li, J. Lightwave Technol. **26**, 1032 (2008).

[5] R.-J. Essiambre, G. Kramer, P.J. Winzer, G.J. Foschini, and B. Goebel, J. Lightwave Technol. **28**, 662 (2010).

[6] Q. Lin, O.J. Painter, and G.P. Agrawal, Opt. Express **15**, 16604 (2007).

[7] R. Dekker, N. Usechak, M. Först, and A. Driessen, J. Phys. D **40**, R249 (2007).

[8] M.A. Foster, A.C. Turner, M. Lipson, and A.L. Gaeta, Opt. Express **16**, 1300 (2008).

[9] J. Chow, G. Town, B. Eggleton, M. Ibsen, K. Sugden, and I. Bennion, IEEE Photon. Technol. Lett. **8**, 60 (1996).

[10] H. Shi, J. Finlay, G.A. Alphonse, J.C. Connolly, and P.J. Delfyett, IEEE Photon. Technol. Lett. **9**, 1439 (1997).

[11] H. Zhang, D.Y. Tang, X. Wu, and L.M. Zhao, Opt. Express **17**, 12692 (2009).

[12] X.M. Liu, D.D. Han, Z.P. Sun, C. Zeng, H. Lu, D. Mao, Y.D. Cui, and F.Q. Wang, Sci. Rep. **3**, 2718 (2013).

[13] E. Iannone, F. Matera, A. Mecozzi, and M. Settembre, *Nonlinear Optical Communication Networks* (Wiley, New York, 1998).

[14] L.F. Mollenauer and P.V. Mamyshev, IEEE J. Quantum Electron. **34**, 2089 (1998).

[15] V.E. Zakharov and A.B. Shabat, Zh. Eksp. Teor. Fiz. **61**, 118 (1971) [Sov. Phys. JETP **34**, 62 (1972)].

[16] Y. Chung and A. Peleg, Nonlinearity **18**, 1555 (2005).

[17] D. Chakraborty, A. Peleg, and Q.M. Nguyen, Opt. Commun. **371**, 252 (2016).

[18] F.M. Mitschke and L.F. Mollenauer, Opt. Lett. **11**, 659 (1986).

[19] J.P. Gordon, Opt. Lett. **11**, 662 (1986).

[20] Y. Kodama and A. Hasegawa, IEEE J. Quantum Electron. **23**, 510 (1987).

[21] A.R. Chraplyvy, Electron. Lett. **20**, 58 (1984).

[22] F. Forghieri, R.W. Tkach, and A.R. Chraplyvy, IEEE Photon. Technol. Lett. **7**, 101 (1995).

[23] S. Chi and S. Wen, Opt. Lett. **14**, 1216 (1989).

[24] B.A. Malomed, Phys. Rev. A **44**, 1412 (1991).

[25] S. Kumar, Opt. Lett. **23**, 1450 (1998).

[26] T.I. Lakoba and D.J. Kaup, Opt. Lett. **24**, 808 (1999).

[27] A. Peleg, Opt. Lett. **29**, 1980 (2004).

[28] Q.M. Nguyen and A. Peleg, J. Opt. Soc. Am. B **27**, 1985 (2010).

[29] C. Headley III and G.P. Agrawal, J. Opt. Soc. Am. B **13**, 2170 (1996).

[30] D.N. Christodoulides and R.B. Jander, IEEE Photon. Technol. Lett. **8**, 1722 (1996).

[31] K.-P. Ho, J. Lightwave Technol. **18**, 915 (2000).

[32] T. Yamamoto and S. Norimatsu, J. Lightwave Technol. **21**, 2229 (2003).

[33] A. Peleg, Phys. Lett. A **360**, 533 (2007).

[34] Y. Chung and A. Peleg, Phys. Rev. A **77**, 063835 (2008).

[35] A. Peleg and Y. Chung, Opt. Commun. **285**, 1429 (2012).

[36] D. Cotter and A.M. Hill, Electron. Lett. **20**, 185 (1984).

[37] M. Muktoyuk and S. Kumar, IEEE Photon. Technol. Lett. **15**, 1222 (2003).

[38] A. Peleg, Phys. Lett. A **373**, 2734 (2009).

[39] C. Xu, X. Liu, and X. Wei, IEEE J. Quantum Electron. **10**, 281 (2004).

[40] A.H. Gnauck and P.J. Winzer, J. Lightwave Technol. **23**, 115 (2005).

[41] V.J. Mazurczyk, G. Shaulov, and E.A. Golovchenko, IEEE Photon. Technol. Lett. **12**, 1573 (2000).

[42] H. Kim, J.H. Lee, and H. Ji, Opt. Express **16**, 20687 (2008).

[43] Q.M. Nguyen and A. Peleg, Opt. Commun. **283**, 3500 (2010).

[44] A. Peleg, Q.M. Nguyen, and Y. Chung, Phys. Rev. A **82**, 053830 (2010).

[45] A. Peleg and Y. Chung, Phys. Rev. A **85**, 063828 (2012).

[46] D. Chakraborty, A. Peleg, and J.-H. Jung, Phys. Rev. A **88**, 023845 (2013).

[47] A. Hasegawa and Y. Kodama, *Solitons in Optical Communications* (Clarendon, Oxford, 1995).

[48] M.N. Islam, ed., *Raman Amplifiers for Telecommunications 1: Physical Principles* (Springer, New York, 2004).

[49] C. Headley and G.P. Agrawal, eds., *Raman Amplification in Fiber Optical Communication Systems* (Elsevier, San Diego, CA, 2005).

[50] L.F. Mollenauer, P.V. Mamyshev, and M.J. Neubelt, Electron. Lett. **32**, 471 (1996).

[51] M. Nakazawa, K. Suzuki, H. Kubota, A. Sahara, and E. Yamada, Electron. Lett. **33**, 1233 (1997).

[52] M. Nakazawa, K. Suzuki, E. Yoshida, E. Yamada, T. Kitoh, and M. Kawachi, Electron. Lett. **35**, 1358 (1999).

[53] M. Nakazawa, IEEE J. Sel. Top. Quant. Electron. **6**, 1332 (2000).

[54] Note that similar perturbed coupled-NLS models with second-order dispersion, Kerr nonlinearity, and delayed Raman response, but without frequency dependent linear gain-loss, were used in Refs. [25, 26].

[55] The dimensionless distance z in Eq. (1) is $z = X/(2L_D)$, where X is the dimensional distance, $L_D = \tau_0^2/|\tilde{\beta}_2|$ is the dimensional dispersion length, τ_0 is the soliton width, and $\tilde{\beta}_2$ is the second-order dispersion coefficient. The dimensionless time is $t = \tau/\tau_0$, where τ is the time. The solitons spectral width is

$\nu_0 = 1/(\pi^2 \tau_0)$ and the interchannel frequency difference is $\Delta\nu = (\pi\Delta\beta\nu_0)/2$. $\psi_j = E_j/\sqrt{P_0}$, where E_j is proportional to the electric field of the jth pulse sequence and P_0 is the peak power. The dimensionless second order dispersion coefficient is $d = -1 = \tilde{\beta}_2/(\gamma P_0 \tau_0^2)$, where γ is the Kerr nonlinearity coefficient. The dimensionless Raman coefficient is $\epsilon_R = 0.006/\tau_0$, where τ_0 is in picoseconds. The dimensionless linear gain-loss coefficients g_j are given by $g_j = 2\tau_0^2\tilde{g}_j/|\tilde{\beta}_2|$, where $\tilde{g}_j$ are the dimensional linear gain-loss coefficients.

[56] Note that the description of the frequency dependent linear gain-loss in terms of a *single* function $g(\omega)$ is the only self-consistent characterization of the linear gain-loss for a *single* fiber.

[57] V. Volterra, "Variations and fluctuations of the number of individuals in animal species living together", translated in *Animal Ecology*, R.N. Chapman, ed., (McGraw-Hill, New York, 1931).

[58] M.W. Hirsch and S. Smale, *Differential Equations, Dynamical Systems, and Linear Algebra* (Academic, New York, 1974).

[59] We point out that similar results are obtained with other choices of the physical parameter values. That is, our results are not very sensitive to the values of J, T, and $\Delta\beta$, as long as $T > 10$ and $\Delta\beta > 10$.

[60] M. Nakazawa, E. Yamada, H. Kubota, and K. Suzuki, Electron. Lett. **27**, 1270 (1991).

[61] A similar but z- and j-independent linear gain-loss function $\tilde{g}(\omega)$ was used in Ref. [17] in a study of pulse propagation in nonlinear waveguide couplers in the absence of delayed Raman response.

[62] The shifting of the central amplification bandwidth of the linear gain-loss (11) is somewhat similar to the shifting of the central frequency in sliding frequency filters, which were widely studied in the context of soliton-based transmission. See Ref. [13] and references therein.

[63] D.J. Kaup, Phys. Rev. A **44**, 4582 (1991).

[64] M. Chertkov, Y. Chung, A. Dyachenko, I. Gabitov, I. Kolokolov, and V. Lebedev, Phys. Rev. E **67**, 036615 (2003).

[65] In the absence of delayed Raman response and linear gain-loss, we employ Eqs. (A.1) and (A.2) with $\eta_j(z) = \eta_j(0)$ and $\beta_j(z) = \beta_j(0)$.